Canadian Science Publishing | Canadian Geotechnical Journal

Towards rational use of baffle arrays on sloped and horizontal terrain for filtering boulders

Journal:	*Canadian Geotechnical Journal*
Manuscript ID	cgj-2020-0363.R2
Manuscript Type:	Article
Date Submitted by the Author:	20-Nov-2020
Complete List of Authors:	Goodwin, Saoirse; Hong Kong University of Science and Technology, Civil and Environmental Engineering Choi, Clarence; Hong Kong University of Science and Technology, Department of Civil and Environmental Engineering Yune, Chan-Young; Gangneung-Wonju National University, The Department of Civil Engineering
Keyword:	landslides, baffles, discrete element method, boulders, impact load
Is the invited manuscript for consideration in a Special Issue? :	Not applicable (regular submission)

General information of the article

Type of paper: Article

Title: Towards rational use of baffle arrays on sloped and horizontal terrain for filtering boulders

Authors: S. R. Goodwin, C.E. Choi*, and C-Y. Yune

Author information:

Co-author: S. R. Goodwin

Postdoctoral fellow, Department of Civil Engineering, The University of Hong Kong, Pokfulam, Hong Kong SAR, China.

E-mail: srgoodwin@protonmail.com

Co-author: C. E. Choi*

Assistant Professor, Department of Civil Engineering, The University of Hong Kong, Pokfulam, Hong Kong SAR, China.

E-mail: cechoi@hku.hk

Co-author: C-Y. Yune

Vice Dean of Planning and Cooperation, The Department of Civil Engineering; Gangneung-Wonju National University, Republic of Korea

E-mail: yune@gwnu.ac.kr

* Corresponding author

Words in abstract: 202

Word count in main text: 6,577

Word count in appendices: 762

Word count in references: 2,489

Figures: 10 (main text) + 2 (appendices)

Tables: 4

Towards rational use of baffle arrays on sloped and horizontal terrain for filtering boulders

S. R. Goodwin[1], C. E. Choi[1 2*], and C-Y. Yune[3]

The Department of Civil Engineering; The University of Hong Kong University, HKSAR, China[1]

The University of Hong Kong Shenzhen Institute of Research and Innovation, Nanshan, Shenzhen, China [2]

The Department of Civil Engineering; Gangneung-Wonju National University, Republic of Korea[3]

Corresponding author *

Abstract

Baffle arrays are used to filter boulders from granular flows, such that the impact load exerted on barriers is reduced. However, current guidelines provide limited recommendations on baffle design. In this study, a calibrated Discrete Element Method modelled boulders entrained in a bulk granular assembly interacting with baffles and a terminal rigid barrier. Different baffle spacings relative to the boulder diameter ($1 < s/\delta < 4$) were considered. A ratio of $s/\delta = 1$ is recommended for reducing the impact load by up to 80%, whilst $s/\delta = 4$ renders an array of baffles inadequate for filtration. The optimum configuration is a staggered array with three rows of baffles on a horizontal plane in front of a barrier. This layout reduces the peak discharge by up to four times more than a similar array on sloping terrain, compared to channels without baffles. Furthermore, the transition from sloping terrain to a horizontal plane works together with the array of baffles to dissipate flow kinetic energy. On the horizontal plane, baffles attenuate the flow velocity more as the Froude number *Fr* increases, implying that baffles should be used if high *Fr* are anticipated. Finally, guidance is provided on estimating load attenuation from boulder filtration.

Keywords: landslides, baffles, discrete element method, boulders, impact load

I. INTRODUCTION

Steep creek hazards in mountainous regions can entrain large boulders (diameter $\delta_{\text{boulder}} \geq 1$ m) (see Alexander and Cooker 2016; Koo *et al*. 2016; Kwan *et al.* 2018). Large barriers are often constructed to arrest geomaterial to avoid it from impacting facilities in mountainous areas, but are prone to damage from large boulders. Solutions to reduce the potential damage from large boulders include installing an array of baffles in front of the barrier.

Baffles are rigid columns which can form an array comprising multiple rows (e.g. VanDine 1996) (Fig. 1), and are installed on slopes (Fig. 1a) or horizontal planes in basins (Fig. 1b). Baffles are intended to (*i*) decelerate flows; and (*ii*) filter out boulders (e.g. NILIM 2007, 2016; Piton and Recking 2016; Kwan *et al.* 2018). Baffle arrays have been widely implemented for landslide mitigation, but designs are prescriptive. Indeed, existing guidelines (e.g. VanDine 1996; Kwan *et al.* 2018) make no link between the placement of baffles with whether baffles are for trapping or controlling discharge. A better understanding is particularly important given potential space constraints at sites, and the cost of installing these obstacles.

Loads on terminal barriers due to boulders are generally considered by (*i*) using Hertzian mechanics to explicitly calculate discrete impacts, or (*ii*) increasing the empirical coefficient α that is applied to the continuum equation for the dynamic pressure. International guidelines lack a consensus for when each approach is appropriate. Nonetheless, GEO (2016) suggests that boulder diameters δ_{boulder} of less than 0.5 m in diameter should be dealt with using continuum mechanics.

For the continuum method, the load can be decomposed into static and dynamic components (e.g. Albaba *et al.* 2018), and written in the form:

$$F_{\text{flow}} = Bh\left(k\rho gh + \alpha\rho U^2\right) \quad (1)$$

where B is the channel width; h is the flow depth; k is an earth pressure coefficient; ρ is the bulk density of the flow material; g is gravitational acceleration; α is a semi-empirical impact coefficient (e.g. Ng *et al.* 2016); and U is the flow velocity. (It is also worthwhile to note that a displacement-based approach, in which the barrier is considered to move upon impact (see Yong *et al.* 2019) is emerging in engineering design practice.)

A challenge for engineers is characterising the reduction in impact load on a terminal barrier for a given geometric configuration of baffles. Kwan *et al.* (2018) mentions $1.5 < s/\delta < 4.0$, where s is the spacing between baffles and δ is the grain diameter, whilst Silva *et al.* (2016) proposes s/δ of almost unity for a columnar array. However, for both cases, the link between α (in Eqn. 1) and s/δ (which does not appear in Eqn. 1) is unclear.

A separate issue is that guidelines do not state whether baffles should ideally be placed on a slope or on the horizontal plane (Table 1), although it is acknowledged that this is sometimes dictated by the constraints of individual sites. Although baffle arrays are often installed on a horizontal plane (Fig. 1b), only Fei *et al.* (2020) has considered a baffle array on a horizontal runout zone. The abrupt transition from a slope to a horizontal plane enhances the dissipation of energy. This energy dissipation is potentially an important factor contributing to the apparent effectiveness of baffles.

Modelling interactions between a flow, boulders and baffles is challenging since multiple mechanisms are involved, many of which are inherently discrete. For instance, jamming can occur if s/δ is sufficiently small; particle size segregation affects the trajectory of boulders (e.g. Zhou and Ng 2010; Song *et al.* 2018); and the formation and destruction of arches at the meso-scale are responsible for localized force fluctuations during impact with obstacles (Faug 2015). Frictional behaviour can occur concurrently with fluid-like behaviour. For example, material can accumulate behind baffles, forming a ramp (e.g. Hákonardóttir *et al.* 2003a, 2003b) whilst other material continues to flow downstream. Since baffles have a finite height, this can enable boulders and other flow material to overtop baffle arrays (Kwan *et al.* 2018). Furthermore, if granular material discharges between baffles at high velocities, fluid-like jets of discharging material undergo mutual interference (Hákonardóttir *et al.* 2003b; Choi et al. 2014; 2015a).

These discrete, coupled mechanisms make it difficult to develop analytic equations to describe flow-boulder-baffle interaction. To understand the impact load on a terminal barrier, it is necessary to model the problem using a discrete approach, as per the majority of studies collected in Table 2. Both physical modelling and numerical tools such as the Discrete Element Method (DEM) can be used.

Some studies have investigated the trapping of boulders impacting columnar arrays for values of s/δ conducive to trapping (e.g. Choi *et al.* 2016 and Goodwin and Choi 2020), whilst others have looked at the load on terminal obstacles shielded by baffles (Law *et al.* 2015 and Bi *et al.* 2018a). However, these studies used approximately monodisperse flow material. Monodisperse flows are a helpful simplification for characterizing the grain diameter, which is relevant for s/δ. However, monodisperse flows may increase the grain-trapping efficiency relative to non-monodisperse flows for a given value of s/δ_{max}. For non-monodisperse flows interacting with an aperture with a given width s, the presence of grains much smaller than the boulders is likely to inhibit stable arch formation. This is because the average ratio of s/δ would be increased to be outside of the range required for trapping (see also Pardo and Sáez 2014).

In this study, a series of physical tests of granular flows impacting a baffle-like structure was performed to calibrate a DEM model. The calibrated DEM model was then used to investigate the effects of the geometric configuration of baffles on the reduction of impact load on a terminal barrier due to boulders entrained by a granular flow. The parameters considered include: (*i*) baffle spacing relative to the boulder diameter (s/δ); and *(ii*) the placement of the baffle array relative to a terminal barrier.

2. METHODOLOGY

2.1 Physical modelling

Physical tests were required to calibrate the numerical model. A modular channel with a rectangular cross-section was used for the physical tests. The channel had a maximum length of 6.0 m, a width of 0.2 m and a height of 0.5 m. Two modules with a combined length of 3.0 m are shown in Fig. 2(a). A baffle-like slit-structure comprising two rigidly fixed planes was placed 0.984 m downstream from the storage area. The planes each had widths of 0.075 m, creating a slit with a width of 0.05 m (Figs. 2(b) and 2(c)). The grain diameter adopted in the experiments was 0.01 m, giving a ratio of s/δ of five. The slit-structure is similar to the opening between a pair of baffles.

A 3D printer was used to print three identical roughened basal plates. The plates each had a width of 200 mm, a length of 208 mm and a depth ranging from 3 mm to 6 mm, giving a height difference of 3 mm between the highest and lowest points. The topography was generated procedurally based on a triangular lattice. The triangles were equilateral and had a side length of 20 mm. Procedural generation (see for example Flaischlen and Wehinger 2019) was selected because it reduces crystallization effects of spherical discrete elements at the base that can otherwise affect flows that are nearly monodisperse (e.g. Marchelli *et al.* 2019). The ratio of the side length of the triangles to the channel width was 1:10. The height difference between the highest and lowest points (of 3 mm) was chosen following Iverson *et al.* (2010), where tests were performed using a bed roughened with protruding cylinders 16 mm in length. The maximum bulk grain diameter in Iverson *et al.* (2010) was 32 mm, giving a ratio of bed to flow grain sizes $\delta_{bed}/\delta_{bulk}$ of less than 0.5. The bulk flow grain diameter adopted in our study was 10 mm, giving a ratio $\delta_{bed}/\delta_{bulk}$ of 0.3. It should be noted that according to Iverson *et al.* (2010) the distinctive behaviour of granular flows (including debris flows) cannot be attributed to a fixed, non-Newtonian rheology, and that this type of morphological boundary friction is critical.

All of the 3D-printed basal plates were covered with adhesive transparent film to ensure that the material interface friction angle was the same as the rest of the flume. The 3D-printed plates are shown in Figs. 2(b) and 2(c). The three roughened plates were placed upstream of the baffle-like slit-structure. The height of the plates was flush with the initial part of the flume channel (Fig. 2(d)). Schematics are shown in Figs. 2(d) and 2(e).

2.2. Discrete element method

The Discrete Element Method (DEM) has been widely adopted for modelling the interaction between flows and obstacles (e.g. Teufelsbauer *et al.* 2009, 2011; Zhao and Shan 2013; Ng *et al.* 2013; Shan and Zhao 2014; Albaba *et al.* 2015; Choi and Law 2015; Law *et al.* 2015; Leonardi *et al.* 2015, 2016, 2019; Shen *et al.* 2018; Marchelli *et al.* 2019; Choi and Goodwin 2020; Zhou *et al.* 2020). The open-source DEM package LIGGGHTS was used (Kloss and Goniva 2011). The forces acting on each grain at each time step were calculated as follows:

$$m_{\mathrm{i}}\frac{\mathrm{d}U_{\mathrm{i}}}{\mathrm{d}t} = F + m_{\mathrm{i}}g \tag{2}$$

In Eqn. (2), m_{i} is the mass of grain i; U_{i} is the velocity of grain i; t is time; F includes all non-gravitational external forces acting on the grain (i.e. contact forces); and g is gravitational acceleration. The acceleration, velocity and position of each grain are calculated sequentially using Newtonian mechanics. For calculating the forces on grains during collisions, a Hertzian (non-linear) contact model was used. (Readers may refer to DCS 2020 for details.) This contact model was chosen since grain interactions are inherently non-linear (Maranzano & Hancock 2016).

The material density was 2650 kg/m^3 which is characteristic of rock, sand and glass. For monodisperse spheres, which have a maximum packing fraction of around 0.6, this gives rise to a bulk density of around 1600 kg/m^3. The elastic modulus E was set at 0.1 GPa (Law *et al.* 2015). Although this value is less than the characteristic value of rock, sand or glass (10 GPa < E < 100 GPa), a more computationally efficient time step can be used. The time step adopted was 5 μs (Law *et al.* 2015). The internal friction angle was 20°, which was back-calculated from the comparison of physical and numerical flow dynamics in Ng *et al.* (2019) and can be considered conservative. The interface friction angle was physically measured for glass beads in Choi *et al.* (2016) using tilt-tests. Poisson's ratio was set at 0.3 as per previous studies (e.g. Law *et al.* 2015). Rolling resistance was set at zero since spheres were being modelled.

The coefficient of restitution (e) determines the energy lost during each collision between objects. In reality the coefficient is a function of the impact velocity (e.g. Lam *et al.* 2018). A value of e of unity implies that the impact is fully elastic, whereas zero implies that the impact is entirely non-elastic. A consequence of higher values of e is that collisions tend to be shorter, which implies that the transient load imparted on a barrier tends to increase, according to:

$$F = \frac{m(U_2 - U_1)}{\Delta t} \tag{3}$$

where m is the mass of the impacting object, U_1 and U_2 are the velocities before and after impact, and Δt is the impact time. Since the value of e for glass is higher than for rock, this implies that the impact load will tend to be higher for the same mass, thus erring on the conservative side.

Indeed, Ng *et al.* (2019) used physical drop tests to characterize the coefficient of restitution of glass beads 10 mm in diameter. These beads impacted a fixed metal slab and had a measured coefficient of restitution of 0.74. Chau *et al.* (1996) tested rock fragments falling onto slopes and found the coefficient of restitution to be between 0.39 and 0.49. Pfeiffer and Bowen (1989) back-analysed the coefficient of restitution for rockfalls considering various bed materials, reporting a range of 0.28 to 0.42, whilst Hungr and Evans (1988) back-analysed a value of 0.5. Choi *et al.* (2015a) and Law *et al.* (2015) also used a value of 0.5 for DEM back-analyses of sand flows. Of these studies, values for the coefficient of restitution nearer the lower end may be more plausible for full-scale modelling. This is because large rocks can dissipate energy through fracturing (Bowman *et al.* 2012). Nonetheless, the coefficient of restitution was set at 0.5 as a maximum plausible value. It should be noted that a value of e that is higher than that for natural geological materials suggests that results from this study should tend to be on the conservative side, in terms of impact load. Numerical parameters are summarised in Table 3.

2.3. Evaluation of numerical parameters

Computed and physical flow kinematics were compared to evaluate the numerical parameters discussed in the previous section. Fig. 3 compares physical and numerical flow kinematics for a flow impacting a slit-structure with a single slit. The DEM channel geometry and grain diameter were identical to the physical experiments. Indeed, the stereolithography (STL) files for the rough basal plates created using the 3D printer were the same ones used in the DEM. A

detailed numerical procedure for back-analyses of small-scale model flume experiments of monodisperse flows is given in both Ng *et al.* (2019) and Goodwin and Choi (2020). This procedure is similar to the procedure detailed in Section 2.6 of this study.

Fig. 3 shows that the DEM model captures the essential kinematics of the interaction between the flow and the slit-structure. Particle Image Velocimetry (PIV) was also performed using the open-source PIV package OpenPIV (Thielicke & Stamhuis 2014) to show the local velocities quantitatively. The granular flow approaches the slit-structure (Fig. 3*i*), and then piles up, forming a ramp (e.g. Hákonardóttir *et al.* 2003b). At the same time, the granular material flows out of the slit as a granular jet (e.g. Hákonardóttir *et al.* 2003b; Choi *et al.* 2015a) (Figs. 3*ii* to 3*v*). The velocity profiles at each time step are qualitatively similar.

A direct comparison of the physically measured and numerically extracted maximum pile-up heights and average outflow rates is given in Figs. 4a and 4b. The values for the pile-up heights are normalized by the maximum flow depth of flows in channels without obstacles (see Choi *et al.* 2016). The depths agree between 89 and 99%. The physical and numerical values for the outflow rates closely follow the same trend, and differ by 6% for the channel inclination adopted in the main part of this study (i.e. 30°). Taken together, Figs. 3 and 4 show that interactions between the flow and the structure are captured well by the numerical DEM model. This lends further confidence to the input parameters.

2.4. Scaling and characterisation of key dimensionless groups

Key scaling groups for granular flows include the Froude number *Fr*, the number of grains per unit depth and the solid volume fraction (Armanini *et al.* 2011, 2014; Armanini 2015). *Fr* gives the ratio of inertial to gravitational forces (Armanini *et al.* 2011, 2014; Armanini 2015; Choi *et al.* 2015b; Ng *et al.* 2016, 2019):

$$Fr = \frac{U}{\sqrt{gh\cos\theta}} \tag{4}$$

where U is the flow velocity; g is gravitational acceleration; h is the flow depth; and θ is the channel inclination. Flows in channels without obstacles were used to characterize the frontal Froude number (Ng *et al.* 2019) to give a clear benchmark for future studies. The placement of baffles on the slope was decided based on the tests without obstacles. This was to ensure that *Fr* before impact was the same as for baffles on the horizontal channel. The methodology and results for this exercise are detailed in Appendix I.

2.5. Numerical domain for main study: boulders, baffles and barriers

The numerical domain is shown in Fig. 5 and consists of several components: a storage area for retaining granular material before dam-break; an initial channel section 3 m in length; a horizontal perch 1 m in length for boulders; a second channel section with a variable length to control *Fr* (details given in Appendix I); and finally a horizontal channel. The channel was inclined at 30°, which is typical of real hillsides (see Kwan 2012 and CEDD 2020).

The base was given a slight morphological roughness using the same method described in the methodology for the calibration exercise. The purposes of this roughness included: (*i*) promoting a limited-slip condition near the base so that the velocity profile of the bulk granular material was closer to that of prototype flows; and (*ii*) promoting bouncing of the boulders, since the motion of boulders on slopes is governed primarily by bouncing (Wyllie 2014). Increasing the degree of roughness further would tend to retard the flow (see Kumaran and Bharathraj 2013), thus reducing the Froude number and reducing the amount of granular material travelling through the baffle array. Decreasing the basal roughness from the amount set in this study makes little difference to the Froude number, but causes rolling to become more important for the motion of the boulders, at the expense of bouncing (see Wyllie 2014). It is worth noting that other authors (e.g. Bryant *et al.* 2015) have also used roughened beds for promoting a limited-slip condition, although the method of roughening varies. Specifically, Bryant *et al.* (2015) used a circular steel mesh on the channel base, but the effect is the same as in our study.

For the tests with obstacles, an array of baffles was added, either on the horizontal channel (Fig. 5a) or on the slope (Fig. 5b). A barrier was placed 9.5 m away from the start of the horizontal channel. The obstacle layout for both cases is shown in Figs. 5c and 5d.

The length for the upper channel section before the perch was determined based on the minimum Froude number required to dislodge the boulders. This was calculated using an expression from Alexander and Cooker (2016) considering drag force, impulsive force, and frictional force:

$$\frac{{U_0}^2}{gh} \geq 2\frac{(V_{\text{boulder}}/A_{\text{boulder}})}{h}\left[\left(\frac{\rho_{\text{s}}}{\rho_f}-1\right)\mu_{\max}-k_{\text{shape}}\frac{a}{g}\right] \quad (5)$$

where U_0 is the velocity before impact; g is the gravitational acceleration; h is the flow depth; V_{boulder} and A_{boulder} are the volume and cross-sectional area of the boulder, respectively; ρ_{s} and ρ_{f} are the densities of the boulder and the bulk granular assembly respectively; $\mu_{\max}$ is the friction angle between the boulder and the channel base; k_{shape} is a shape-dependent parameter, and is 0.5 for spherical boulders; and a is the flow acceleration during interaction with the

boulder. For the purposes of Eqn. (5), the bulk granular assembly was idealised as an equivalent fluid. It is nonetheless acknowledged that the flow regime is frictional rather than inviscid. Taking $V = 0.52$ m^3, $A = 0.79$ m^2 (for boulders 1 m in diameter), $h = 1$ m, $\rho_s = 2650$ kg/m^3, $\rho_f = 1600$ m^3 and $\mu_{max} = 0.37$, the threshold for Fr was calculated to be 0.3. As such, any flow with $Fr > 0.3$ should be able to entrain the perched boulders. For the flows performed in this study, Fr at the flow front on the perch was around 2.

Grains in the bulk granular assembly had a diameter of 0.2 m, whilst the boulders had a diameter of 1 m. The initial bulk volume was around 85 m^3. The volume of material is characteristic of small landslides in Hong Kong and was conducive to the general range of Froude numbers of debris flows, specifically $0 < Fr < 7.5$ (Hübl *et al.* 2009). The characterisation of the Froude number for the flow front is given in Appendix I. The bulk grain size was chosen such that the ratio s/δ for the bulk assembly was large enough that jamming was unlikely to occur if boulders were not present (see also findings from Law et al. 2015, Choi et al. 2016 and Goodwin and Choi 2020). If the ratio s/δ is high enough for trapping not to occur, the main influence of the grain size in the bulk granular assembly relates to energy dissipation during transportation (Ng *et al.* 2017), and hence the flow Froude number.

2.6. Numerical procedures

Dam break, which is a well-established technique for initiating model flow-type landslides, including granular flows, was adopted in this study (see Iverson 2015, as well as Iverson *et al.* 2010; Ashwood & Hungr 2016). Granular material was generated within the inclined storage area and allowed to settle (see Fig. 5). The gate was then deleted, allowing granular material to flow downstream into the boulders, entraining them. The flow and boulders then moved towards the baffle array. The simulation was terminated after impact, once the system energy fell below a certain threshold (around 0.1 % of the maximum kinetic energy of the entire system of grains that was recorded during outflow). It was found that the boulders had always stopped moving by the time this threshold was reached. Furthermore, it is acknowledged that it would also be possible to terminate the simulations on conditions relating to unbalanced forces (e.g. Wang *et al.* 2019), although is observed that such conditions are generally applied to quasi-static problems (e.g. Ng et al. 2015; Wang *et al.* 2019). It was found that the boulders had always stopped moving by the time this threshold was reached.

2.7. Test plan

The baffle array was based on the configuration discussed in Kwan *et al.* (2018). Baffles with sides of 1.0 m and heights of 1.5 m on the upstream face were installed. Rows of baffles were spaced by 1.5 m (Kwan *et al.* 2018). Three rows of baffles were selected as per Law *et al.* (2015). Rows of baffles were staggered (Cosenza *et al.* 2006; Teufelsbauer *et al.* 2011; Choi *et al.* 2014, 2015a; Ng *et al.* 2015; Law *et al.* 2015; Wang *et al.* 2019a, 2019b; Bi *et al.* 2018a, 2018b; Kwan *et al.* 2018; Kim *et al.* 2019; Fei *et al.* 2020; Li *et al.* 2020). Furthermore, a range of lateral baffle spacings of $1 < s/\delta < 4$ was investigated, covering the range mentioned in Kwan *et al.* (2018). Table 4 summarises the test plan.

3. INTERPRETATION OF RESULTS

3.1. Observed flow kinematics

Fig. 6 shows side and top-down views of the channel and barrier. The array of baffles is installed on the slope in Fig. 6a and in the horizontal channel in Fig. 6b. The spacing s/δ is 1 in both cases.

In Fig. 6a(*i*), boulders have been entrained by the flow front. Fig. 6a(*ii*) shows pile-up and overflow for the bulk granular assembly occurring; all of the boulders have impacted the baffles, albeit different rows. Figs. 6a(*iii*) to (*v*) show that the bulk granular assembly continues to flow downstream, whilst the boulders have become trapped. Evidently, the baffles are successful at regulating the outflow. Fig. 6a(*vi*) shows the boulders being filtered by the baffles.

In Figs. 6b(*i*) and 6b(*ii*), the boulders and flow are moving downstream towards the baffle array. Fig. 6b(*iii*) shows the boulders impacting the first row of baffles. At the same time, granular jets (e.g. Hákonardóttir *et al.* 2003b) pass between the baffles. Pile-up is observable in Figs. 6b(*iv*) and (*v*), with two boulders overtopping the first row of baffles. Fig. 6b(*vi*) shows the simulation after the material has come to rest. The remnants of granular jets are visible between the final row of baffles and the barrier, but no boulders have reached the terminal barrier.

Overall, Fig. 6 shows that baffles on the slope and on the horizontal may both be effective at reducing the impact load on the barrier due to boulders. The baffles installed on the slope appear to be effective at flow regulation, since a large volume of granular material passes through them. In contrast, a much smaller volume of material passes the baffles in the horizontal channel due to the dissipation of flow kinetic energy at the transition between the slope and the horizontal plane.

3.2 Flow velocity and flow rate of material passing through an array of baffles

Fig. 7 shows averaged velocities for flow material passing through arrays of baffles, normalised by averaged velocities for flows without obstacles. Fig. 7a shows that this normalised velocity increases as Fr increases and as s/δ decreases. The increase with Fr is because of the increasing importance of overflow. The dependence on overflow is qualitatively inferable from the formulations for pile-up height for flows impacting a rigid barrier given in Jóhannesson *et al.* (2009), Choi *et al.* (2015c) and Iverson *et al.* (2016). As such, studies or recommendations that give baffle height solely in terms of the flow depth (e.g. Hákonardóttir *et al.* 2003b, Choi *et al.* 2014; Kwan *et al.* 2018) may potentially lead to designs that lead to overflow. Thus, Fr must also be considered in the design of baffles.

Assuming steady-state conditions are applicable, it is expected that the flow velocity should increase as the baffle spacing is decreased (Choi *et al.* 2015a). This is because constrictions tend to maintain a constant overall flow rate Q, according to $Q = UA_{\text{flow}}$, where A_{flow} is the cross-sectional area of the flow. This effect diminishes as Fr becomes lower due to the lack of momentum driving the flow through the slits between baffles. Other studies such as Hákonardóttir *et al.* (2003b) and Choi *et al.* (2014) report net reductions in velocity (see also Table 2). The apparent differences with results from this study may be because of the way that Fr is characterized: the velocity and flow depth vary continuously across the length of each flow (Ng *et al.* 2019), so direct comparisons of velocity and Fr are not always straightforward.

Fig. 7b shows that after the third row of baffles, the velocity reduction is almost identical to that in Fig. 7a. This is because the increase in flow velocity due to the effects of the constriction is attenuated when the discharge impacts the staggered baffles in the next row, offsetting an increase in velocity due to gravitational acceleration.

Figs. 7c and 7d show that for baffles in the horizontal channel, the effect on the flow velocity due to the constriction size still seems to hold, with more narrowly-spaced baffles producing higher velocities relative to an open channel. However, in contrast to Figs. 7a and 7b, increasing Fr reduces the relative velocity. For $s/\delta = 4$ and $Fr = 3.4$, the relative velocity is around unity, but for $Fr = 4.9$, the relative velocity drops to 0.5. This is because of the influence of the transition (from the slope to the horizontal channel) on the flow velocity. For lower values of Fr (< 4) for channels without baffles, flows become completely arrested on the horizontal channel shortly after the transition from the slope. Evidently, the baffles make little difference. In contrast, for higher Fr (> 4), the flow keeps on moving downstream even after

the transition. This suggests that the beneficial effects of baffles for reducing the flow velocity increase with *Fr*. As such, baffles should be given higher priority during engineering design if higher *Fr* are anticipated, site constraints notwithstanding.

For comparison, Salm (1987) reported that energy dissipation due to baffle-like obstacles is 50% of the transverse blockage, implying a velocity reduction of between 10% for $s/\delta = 4$ to 30% for $s/\delta = 1$. Jóhannesson *et al.* (2009) suggested that a single row of baffles should reduce the flow velocity by 20%, with two rows of baffles reducing it by a further 10%, based on physical experiments using snow where $3 < Fr < 6$. Ng *et al.* (2015) reported a reduction in velocity of between 30 and 60% for dry sand flows impacting three rows of baffles for $Fr \sim 3$. Kim *et al.* (2019) reported a velocity reduction of between 45 and 70% for two-phase flows impacting one to four rows of baffles for $Fr \sim 6$. Wang *et al.* (2019a, 2019b) reported velocity reductions of 3 to 39% for two-phase flows impacting three rows of baffles for $Fr \sim 4$. The wide range of reduction factors reported is interesting, and is probably caused by a range of factors, including s/δ and *Fr* (see the range of values recorded in Table 2).

Fig. 8 shows the normalized peak outflow rate for different cases. The normalized peak outflow rate implicitly accounts for the effects of the transverse blockage on the amount of material that flows downstream. The peak outflow rate for cases with baffles is normalised by that for flows without obstacles at a given static monitoring section (indicated in the insets). Figs. 8a and 8b correspond to monitoring regions behind the first and third rows of baffles, respectively. Two sets of lines are shown on each graph, corresponding to (*i*) different ratios of s/δ and (*ii*) different positions of the baffle array.

Fig. 8a shows that immediately after the first row of baffles, the normalized peak outflow rate increases with *Fr* for $Fr > 3$, regardless of s/δ and the placement of the baffle array. This is due to overflow that occurs for $Fr > 3$. The normalized peak outflow rate for baffles on the slope is generally lower than for baffles in the channel for a given value of s/δ. This reflects that the transition to the horizontal section of channel causes a substantial dissipation of energy (see also Fig. A1a). This dissipation of energy accounts for much of the reduction in the peak outflow rate. This is why the reduction in the outflow rate due to the presence of baffles is less obvious for the horizontal section of the channel than the slope, at least for s/δ of 2 and 4.

Notably, the relationship between s/δ and the peak normalized outflow rate is opposite to that between s/δ and the normalized averaged outflow velocity (see Fig. 7). This is because although the slits cause some material to be accelerated, the actual volume of material passing downstream is rather limited, especially for $s/\delta = 1$. This also suggests why flow velocities

appear to increase in this study but decrease in others (see Hákonardóttir *et al.* 2003b; Jóhannesson *et al.* 2009; Ng *et al.* 2015; Kim *et al.* 2019; Wang *et al.* 2019a, 2019b): for the flow as a whole interacting with baffles, the average velocity for the flow material decreases, but the frontal material passing through the slits accelerates. This is why staggered rows of baffles are required to intercept this accelerated material.

Fig. 8b shows that the peak normalized outflow rate diminishes as flow material passes through additional rows of baffles. For baffles placed on the horizontal plane and $s/\delta = 1$, the discharge rate is less than 10% of the flows in channels without obstacles. For baffles on the slope, the same s/δ reduces the discharge rate by between 25% and 40%. This suggests that the transition and the baffle array together cause a greater degree of energy dissipation than either one on their own, after the flow has passed three rows of baffles. This underscores the importance of accounting for the effects of a transition from the slope to the horizontal, which current international guidelines do not explicitly consider (VanDine 1996; Kwan *et al.* 2018; see Table 1). The increasing reduction in outflow rate as the flow passes more and more rows of baffles also emphasises the need for multiple rows of staggered baffles.

3.3. Mesoscopic behaviour of flows passing through baffle arrays

Filtering boulders fundamentally depends on mesoscopic interactions. Quantities such as the Savage number N_{Sav} (Iverson 1997) differentiate between governing mechanisms of mesoscopic grain interaction, specifically frictional and collisional regimes. However, N_{Sav} is primarily applicable for flows in channels without obstacles, where the grain size is approximately monodisperse.

Instead of the Savage number N_{Sav}, a simple metric of contact durability (Goodwin and Choi 2020) was adopted to characterise the mesoscopic flow behaviour. The contact durability gives the proportion of contacts between grains that are maintained from one time step to the next. Lower values correspond to more frictional flows, whilst higher values correspond to more collisional flows. The calculation process is given in Appendix II. In Fig. 9, the contact durability for flows interacting with a baffle array is normalised by that of the durability of the flow in a channel without obstacles. Sub-unity indicates that flows in channels without obstacles behave more frictionally than flows interacting with baffles; unity indicates similar flow regimes; whilst super-unity indicates that flows in channels without obstacles behave more collisionally than flows interacting with baffles. The abscissa is given as normalised time; the characteristic timescale is the baffle array length L divided by the pre-impact flow velocity U.

For baffles on the slope, the normalised contact durability is initially sub-unity, since grains scatter collisionally after initially impacting the baffles. Thereafter, the value rises: baffles constrict the flow, mobilising frictional shearing. Nonetheless, the normalised contact durability is unity for $Fr = 3.34$ and only slightly super-unity for $Fr = 4.37$. For baffles on the horizontal zone, however, the normalised contact durability rises by more than three times after four normalised time units as the baffles cause the flow to become arrested. This is consistent with the reduction in relative velocity and outflow rate for baffles on the horizontal plane shown in previous figures.

3.4 Reduction of peak load on the terminal barrier due to the presence of an array of baffles

For engineering design, the peak impact loads on a terminal barrier for a variety of Fr and s/δ are of primary interest. Peak loads comprise both continuum and discrete components. The peak loads are normalised by the theoretical static load $Bk\rho gh^2$ (Faug 2015). This also enables theoretical reference lines to be shown: assuming the flows behave as continua, all terms from Eqn. (1) can be scaled by the theoretical static load (Faug 2015):

$$\frac{F}{Bk\rho gh^2} = 1 + \frac{\alpha U^2}{kgh} \tag{6}$$

Eqn. (6) can then be rewritten in terms of Fr:

$$\frac{F}{F_{\text{static}}} = 1 + \frac{\alpha}{k} Fr^2 \tag{7}$$

where B is the channel width; k is an earth-pressure coefficient; ρ is the flow density; g is gravitational acceleration; h is the flow depth; α is an impact coefficient; and Fr is the Froude number. The coefficient α is suggested as being as high as 2.5 in Kwan (2012) to account for the presence of boulders less than 0.5 m in diameter. Although the boulders in this study are larger than 0.5 m, in this discussion we lump them into α for the purposes of easily comparing the effects of different baffle configurations. Taking k as unity, lines for α/k based on Eqn. (7) from 0.5 to 5.0 are shown in Fig. 10.

Fig. 10a shows normalized peak impact loads for $1 < s/\delta < 4$ for baffles installed on the slope. Fr corresponds to the value at the flow front, before impact with the baffle array (see Appendix I). The load on the barrier for $s/\delta = 4$ lies outside even the bound of $\alpha/k = 5.0$. This suggests that $s/\delta = 4$, the upper bound mentioned in both MLR (2004) and Kwan *et al.* (2018), may not be suitable for the purpose of filtering boulders. At most, such a baffle spacing could be adopted for moderate flow rate regulation (see Fig. 8).

For the smallest baffle spacing considered, $s/\delta = 1$, the computed impact load on the barrier is bounded by $\alpha/k = 0.5$, implying that the coefficient α in Eqn. (1) could be reduced for a sufficiently narrow baffle spacing. A coefficient of 0.5 is five times less than that currently suggested for rigid barriers resisting flows with a smaller boulder size of less than 0.5 m (Kwan 2012), implying that the thickness of the barrier could potentially be reduced by a factor of five. The cost savings from the reduction in materials used in the barrier would more than offset those used for the baffles, which generally have a much smaller total volume than terminal barriers (Kwan *et al.* 2018).

Fig. 10b shows similar data as Fig. 10a, but for baffles on the horizontal channel. The impact force due to the boulders on the barrier for $s/\delta = 4$ increases with Fr. The impact forces are higher than the theoretical lines for $\alpha/k = 2.5$ because overflow also increases with Fr, implying that this configuration of baffles is ineffective at reducing load on the terminal barrier. For $s/\delta = 1$, the impact forces lie within the bound $\alpha/k = 0.5$, suggesting that the baffles are successfully able to filter the boulders across a range of Fr. It is worth mentioning that $s/\delta = 1$ was able to filter at least 80% of the boulders for all cases run (i.e. at least 80% of the boulders were not able to pass out of the baffle array). A ratio of $s/\delta = 2$ filtered at least 60% of the boulders, whilst $s/\delta = 4$ filtered at least 20%.

In summary, baffle spacings at the upper bound of $s/\delta = 4$ (mentioned in both MLR 2004 and Kwan *et al.* 2018) are less appropriate for filtering boulders compared to narrower spacings. It is expected that for high values of s/δ, extra rows of baffles would be required to attain the same trapping efficiency as for lower s/δ. Furthermore, baffles on a slope have shown to be less effective at reliably filtering boulders than baffles in a horizontal channel, for given values of Fr and s/δ.

4. CONCLUSIONS

Current recommendations suggest that the ratio between baffle spacing s and boulder diameter δ can be in the range $1 < s/\delta < 4$. However, there is little guidance on the optimal placement of baffles or what conditions enable boulders to be filtered. As such, it is unclear how the impact loading requirements for terminal barriers could be reduced.

The Discrete Element Method (DEM) was used to investigate: (*i*) the placement of the baffle array relative to a rigid barrier; and (*ii*) the baffle spacing relative to the boulder diameter (s/δ). The key conclusions from the simulations performed in this study are as follows:

1) For a baffle spacing of $s/\delta = 1$, the impact coefficient α for the terminal barrier can be reduced to 0.5 for baffles on the slope, or even less for baffles on a horizontal plane, from a nominal value of at least 2.5 for a rigid barrier without baffles. This is because closely-spaced baffles enhance contacts between grains and dissipate flow kinetic energy. For the upper bound of $s/\delta = 4$ mentioned in existing guidelines, the equivalent α can be as high as 5 or more, indicating that such a configuration is unable to filter boulders.
2) Three rows of baffles on a horizontal plane are more effective at reducing flow discharge compared to three rows of baffles on slopes. For $s/\delta = 1$, the third row of baffles on the horizontal plane reduces the peak discharge by up to around 90% relative to a channel without obstacles, whereas the same array of baffles on the slope reduces discharge by up to 75%. This reflects the beneficial effects from the transition between the slope and the horizontal, which enhances the dissipation of flow kinetic energy in concert with the baffle array – more so than either the baffle array or the transition would achieve on their own. Furthermore, increasing s/δ causes the peak discharge to increase proportionately more for baffles on the slope than for baffles on a horizontal plane. The maximum reduction in the peak discharge is up to four times more for baffles on the horizontal plane than a similar array on sloping terrain, compared to channels without baffles.

Acknowledgements

The authors are grateful for the generous financial sponsorship from the National Natural Science Foundation of China (51709052), as well as the Research Grants Council of Hong Kong (16212618; 16209717; 16210219; T22-603/15N; AoE/E-603/18), the Ministry of Land, Infrastructure and Transport of the Korean Government (20RITD-C158631-01) and the

University of Hong Kong start-up fund for new staff from the Department of Civil Engineering and the Faculty of Engineering.

REFERENCES

Albaba, A., Lambert, S., Nicot, F. and Chareyre, B. 2015. Relation between microstructure and loading applied by a granular flow to a rigid wall using DEM modelling. Granular Matter, **17**(5): 603–616.

Albaba, A., Lambert, S. and Faug, T. 2018. Dry granular avalanche impact force on a rigid wall: analytic shock solution versus discrete element simulations. Physical Review E, **97**: 052903.

Alexander, J., and Cooker, M. J. 2016. Moving boulders in flash floods and estimating flow conditions using boulders in ancient deposits. Sedimentology, **63**(6): 1582–1595.

Armanini, A., Larcher, M. and Odorizzi, M. 2011. Dynamic impact of debris flow front against a vertical wall. In: Proceedings of the 5th International Conference on Debris-Flow Hazards Mitigation: Mechanics, Prediction and Assessment 2011, p. 1041–1049.

Armanini, A., Larcher, M., Nucci, E. and Dumbser, M. 2014. Submerged granular channel flows driven by gravity. Advances in Water Resources, **63**: 1–10.

Armanini A. 2015. Closure relations for mobile bed flows in a wide range of slopes and concentrations. Advances in Water Resources, **81**: 75–83.

Ashwood, W. and Hungr, O. 2016. Estimating total resisting force in flexible barrier impacted by a granular avalanche using physical and numerical modelling. Canadian Geotechnical Journal, **53**(10): 1700–1717.

Bi, Y., Du, Y., He, S., Sun, X., Wang, D., Li, X., Liang, H. and Wu, Y. 2018a. Numerical analysis of effect of baffle configuration on impact force exerted from rock avalanches. Landslides, **15**: 1029–1043.

Bi, Y., He, S., Du, Y., Sun, X. and Li, X. 2018b. Effects of the configuration of a baffle-avalanche wall system on rock avalanches in Tibet Zhangmu: discrete element analysis, Bulletin of Engineering Geology and the Environment **4**: 1–16. DOI: 10.1007/s10064-018-1284-8.

Bryant, S. K., Take, W. A., and Bowman, E. T. 2015. Observations of grain-scale interactions and simulation of dry granular flows in a large-scale flume. Canadian Geotechnical Journal **52**(5): 638–655.

Bowman, E. T., Take, W. A., Rait, K. L. and Hann, C. 2012. Physical models of rock avalanche spreading behaviour with dynamic fragmentation. Canadian Geotechnical Journal, **49**(4): 460–476.

CEDD (Civil Engineering and Development Department). 2020. Natural Terrain in Hong Kong. URL: https://hkss.cedd.gov.hk/hkss/eng/natural_terrain.aspx. Civil Engineering and Development Department, Government of the Hong Kong Special Administrative Region, Hong Kong SAR, China PRC.

Chau, K. T., Wong, R. H. C., and Lee, C. F. 1996. Rockfall problems in Hong Kong and some new experimental results for coefficients of restitution. International Journal of Rock Mechanics and Mining Sciences and Geomechanics, **35**(4–5): 662–663.

Choi, C. E., Ng, C. W. W., Song, D., Kwan, J. S. H., Shiu, H. Y. K., Ho, K. K. S., and Koo, R. C. H. 2014. Flume investigation of landslide debris-resisting baffles. Canadian Geotechnical Journal, **51**(5): 540–553.

Choi, C. E., and Law, R. P. H. 2015. Performance of landslide debris-resisting baffles. HKIE Transactions, Special Issue with Award and Shortlisted Papers from HKIE Outstanding Paper Award for Young Engineers/Researchers, **22**(4): 235–246.

Choi, C. E., Ng, C. W. W., Law, R. P. H., Song, D., Kwan, J. S. H., and Ho, K. K. S. 2015a. Computational investigation of baffle configuration on impedance of channelized debris flow. Canadian Geotechnical Journal, **52**(2): 182–197.

Choi, C. E., Ng, C. W. W., Au-Yeung, S. C. H., and Goodwin, S. R. 2015b. Froude characteristics of both dense granular and water flows in flume modelling. Landslides, **12**(6): 1197–1206.

Choi, C. E., Au-Yeung, S. C. H., Ng, C. W. W., and Song, D. 2015c. Flume investigation of landslide granular debris and water run-up mechanisms. Géotechnique Letters, **5**(1): 28–32.

Choi, C. E., Goodwin, S. R., Ng, C. W. W., Cheung, D. K. H., Kwan, J. S. H., and Pun, W. K. 2016. Coarse granular flow interaction with slit-structures. Géotechnique Letters, **6**: 267–274.

Choi, C. E. and Goodwin, S. R. 2020. Interaction between granular flows and flexible obstacles: a grain-scale investigation. Computers and Geotechnics, **128**: 103800. DOI: 10.1016/j.compgeo.2020.103800

Cosenza, E., Cozzolino, L., Pianese, D., Fabbrocino, G., and Acanfora, M. 2006. Concrete structures for mitigation of debris-flow hazard in the Montoro Inferiore Area, Southern Italy. 2nd International Congress, IFSC, Naples, pp 1–12.

DCS Computing. LIGGGHTS User Manual: "gran model hertz model" (online) 2020. URL: https://www.cfdem.com/media/DEM/docu/gran_model_hertz.html (Accessed on 19/11/2020).

Faug, T. 2015. Depth-averaged analytic solutions for free-surface granular flows impacting rigid walls down inclines. Physical Review E, **92**: 062310.

Fei, J., Jie, Y., Sun, X., and Chen, X. 2020. Experimental investigation on granular flow past baffle piles and numerical simulation using a μ(I)-rheology-based approach. Powder Technology, **359**: 36–46.

FHA (Federal Highway Administration, US Department of Transportation). Hydraulic design of energy dissipators for culverts and channels. Hydraulic Engineering Circular No. 14, Third Edition. Publication No. FHWA-NHI-06-086. 2006.

Flaischlen, S. and Wehinger, C. D. 2019. Synthetic packed-bed generation for CFD simulations: Blender vs. STAR-CCM+. Chemical Engineering, **3**(52): 1–22. DOI: 10.3390/chemengineering3020052

Geotechnical Engineering Office (GEO) 2016. GEO Technical Guidance Note No. 47 (TGN 47). Updates of Design Guidance of Rigid Debris-resisting Barriers. Geotechnical Engineering Office, Civil Engineering and Development Department. The Government of the Hong Kong Special Administrative Region.

Goodwin, S. R., and Choi, C. E. 2020. Slit structures: Fundamental mechanisms of mechanical trapping of granular flows. Computers and Geotechnics, **119**: 103376.

Hákonardóttir, K. M., Hogg, A. J., Jóhannesson, T., Kern, M., and Tiefenbacher, F. 2003a. Large-scale avalanche braking mound and catching dam experiments with snow: a study of the airborne jet. Surveys in Geophysics, **24**(5–6): 543–554.

Hákonardóttir, K. M., Hogg, A. J., Jóhannesson, T., and Tómasson, G. G. 2003b. A laboratory study of the retarding effects of braking mounds on snow avalanches. Journal of Glaciology, **49**(165): 191–200.

Hübl, J., Suda, J., Proske, D., Kaitna, R., and Scheidl, C. 2009. Debris flow impact estimation. In: Proceedings of the 11th International Symposium on Water Management and Hydraulic Engineering 2009, p. 137–148.

Hungr, O., and Evans, S. G. 1998. Engineering evaluation of fragmental rockfall hazards. *In* Proceedings of the 5th International Symposium on Landslides, Lusanne. **1**: 685–690.

Iverson, R. M. 1997. The physics of debris flows. Reviews of Geophysics, **35**(3): 245–296.

Iverson, R. M., Logan, M., LaHusen, R. and Berti, M. 2010. The perfect debris flow? Aggregated results from 28 large-scale experiments. JGR Earth Science, **115**(F3). DOI: 10.1029/2009JF001514.

Iverson, R. M. 2015. Scaling and design of landslide and debris-flow experiments. Geomorphology, **244**: 9–20.

Iverson, R. M. George, D. L., and Logan, M. 2016. Debris flow run-up on vertical barriers and adverse slopes. Journal of Geophysical Research: Earth Surface, **121**: 2333–2357.

Jóhannesson, T., Gauer, P., Issler, D., and Lied, K. 2009. The design of avalanche protection dams recent practical and theoretical developments. European Commission, Belgium.

Kim, B-J., Han, K-D., Kim, H-S., Choi, C. E., and Yune, C-Y. 2019. An experimental study on cylindrical countermeasures for dissipation of debris flow energy. Journal of the Korean Geo-Environmental Society, **20**(1): 57–65. (In Korean).

Kloss, C., and Goniva, C. 2011. LIGGGHTS – a new open source discrete element simulation software. In: Proceedings of the 5th International Conference on Discrete Element Methods p. 25–26.

Koo, R. C. H., Kwan, J. S. H., Lam, C., Ng, C. W. W., Yiu, J., Choi, C. E., Ng, A. K. L., Ho K. K. S. and Pun, W. K. 2016. Dynamic response of flexible rockfall barriers under different loading geometries. Landslides, **14**(3): 905–916.

Kumaran, V., and Bharathraj, S. 2013. The effect of base roughness on the development of a dense granular flow down an inclined plane. Physics of Fluids, **25**, 070604.

Kwan, J. S. H. 2012. Supplementary technical guidance on design of rigid debris-resisting barriers, GEO Report No. 270, 2012. Hong Kong, China: Geotechnical Engineering Office, Civil Engineering and Development Department, The HKSAR Government.

Kwan, J. S. H., Koo, R. C. H., and Lam, C. 2018. A review on the design of rigid debris-resisting barriers. GEO Report No. 339, 2018. Hong Kong, China: Geotechnical Engineering Office, Civil Engineering and Development Department, The HKSAR Government.

Lam, N. T. K., Yong, A. C. Y., Lam, C. Kwan, J. S. H., Perera, J. S., Disfani, M. M. and Gad, E. 2018. Displacement-based approach for the assessment of overturning stability of rectangular rigid barriers subjected to point impact. Journal of Engineering Mechanics, **114**(2): 04017161.

Law, R. P. H., Choi, C. E., and Ng, C. W. W. 2015. Discrete element investigation of the influence of granular debris flow baffles on rigid barrier impact. Canadian Geotechnical Journal, **53**(2): 179–185.

Leonardi, A., Wittel, F. K., Mendoza, M., and Herrmann, H. J. 2015. Lattice-Boltzmann method for geophysical plastic flows. Recent Advances in Modeling Landslides and Debris Flows (book), 131–140.

Leonardi, A., Wittel, F. K., Mendoza, M., Vetter, R., and Herrmann, H. J. 2016. Particle–fluid–structure interaction for debris flow impact on flexible barriers. Computer-Aided Civil and Infrastructure Engineering **31**(5): 323–333.

Leonardi, A., Pirulli, M., Yune, C. Y., and Choi, C. E. 2018. Study of the influence of baffles on an artificial debris flow through back-analysis simulations. Second JTC1 Workshop on Triggering and Propagation of Rapid Flow-like Landslides, Hong Kong 2018.

Leonardi, A., Goodwin, S. R., and Pirulli, M. 2019. The force exerted by granular flows on slit-dams. Acta Geotechnica, **14**: 1949–1963. DOI: 10.1007/s11440-019-00842-6.

Li, X., Yan, Q., Zhao, S., Luo, Y., Wu, Y., and Wang, D. 2020. Investigation of influence of baffles of landslide debris mobility by 3D material point method. Landslides, **17**: 1129–1143. DOI: 10.1007/s10346-020-01346-1.

Maranzano, B. J. and Hancock, B. C. 2016. Quantitative analysis of impact measurements using dynamic load cells. Sensing and Bio-Sensing Research **7**: 31–37.

Marchelli, M., Leonardi, A., Pirulli, M., and Scavia, C. 2019. On the efficiency of slit-check dams in retaining granular flows. Géotechnique, **70**(3): 226–237. DOI: 10.1680/jgeot.18.p.044.

MLR (Ministry of Land and Resources) Design Standards for Debris Flow Hazard Mitigation Measures (DZ/T0239-2004). 2004. Ministry of Land and Resources of the People's Republic of China, China. (In Chinese).

Ng, C. W. W., Choi, C. E., and Law, R. P. H. 2013. Longitudinal spreading of granular flow in trapezoidal channels. Geomorphology, **194**: 84–93.

Ng, C. W. W., Choi, C. E., Kwan, J. S. H., Koo, R. C. H., Shiu, H. Y. K., and Ho, K. K. S. 2014. Effects of baffle transverse blockage on landslide debris impedance. Procedia Earth and Planetary Science, **9**: 3–13.

Ng, C. W. W., Choi, C. E., Song, D., Kwan, J. S. H., Koo, R. C. H., Shiu, H. Y. K., and Ho, K. K. S. 2015. Physical modeling of baffles influence on landslide debris mobility. Landslides, **12**(1): 1–18.

Ng, C. W. W., Choi, C. E., Koo, R. C. H., Goodwin, S. R., Song, D., and Kwan, J. S. H. 2018. Dry granular flow interaction with dual-barrier systems. Géotechnique **68**(5): 386–399.

Ng, C. W. W., Choi, C. E., Liu, L. H. D., Wang, Y., Song, D., and Yang, N. 2017. Influence of particle size on the mechanism of dry granular run-up on a rigid barrier. Géotechnique Letters, **7**: 79–89.

Ng, C. W. W., Choi, C. E., and Goodwin, S. R. 2019. Froude characterisation for single-surge unsteady dry granular flows: impact pressure and run-up height. Canadian Geotechnical Journal, **56**(12): 1968–1978. DOI: 10.1139/cgj-2018-0529.

Ng, T.-T., Zhou, W., Ma, G. and Chang, X.-L. 2015. Damping and particle mass in DEM simulations under gravity. Journal of Engineering Mechanics, **141**(6): 04014167.

NILIM (National Institute for Land and Infrastructure Management) Manual of technical standard for establishing Sabo master plan for debris flow and driftwood, Technical Note of NILIM No. 364, 2007. Tsukuba, Japan: National Institute for Land and Infrastructure Management, Ministry of Land, Infrastructure and Transport, Japan. (In Japanese).

NILIM (National Institute for Land and Infrastructure Management). 2016. Manual of technical standard for designing Sabo facilities against debris flow and driftwood. 2016, Japan, TN/905. (In Japanese).

Pardo, G. S., and Sáez, E. 2014. Experimental and numerical study of arching soil effect in coarse sand. Computers and Geotechnics, **57**: 75–84.

Pfeiffer, T. J., and Bowen, T. D. 1989. Computer Simulation of Rockfalls. Bulletin of Association of Engineering Geologists, **26**(1): 135–146.

Piton, G., and Recking, A. 2016. Design of sediment traps with open check dams. I: hydraulic and deposition processes. Journal of Hydraulic Engineering (ASCE) **142**(2): 04015045.

Salm, B. 1987. Snow, avalanches and avalanche protection (lecture notes). Swiss Federal Institute of Technology in Zurich. [In German.]

Shan, T., and Zhao, J. 2014. A coupled CFD-DEM analysis of granular flow impacting on water reservoir. Acta Mechanica, **225**(8): 2449–2470.

Shen, W., Zhao, T., Zhao, J., Dai, F., and Zhou, G. G. D. 2018. Quantifying the impact of dry debris flow against a rigid barrier by DEM analyses. Engineering Geology, **241**: 86–96.

Silva, M., Costa, S., Canelas, R. B., Pinheiro, A. N. and Cardoso, A. H. 2016. Experimental and numerical study of slit-check dams. Int. J. Sustain. Dev. Plan., **11**(2): 107–118.

Song, D., Choi, C. E., Zhou, G. G. D., Kwan, J. S. H., and Sze, H. Y. 2018. Impulse load characteristics of bouldery debris flow impact. Géotechnique Letters, **8**: 111–117.

Teufelsbauer, H., Wang, Y., Chiou, M. C., and Wu, W. 2009. Flow-obstacle-interaction in rapid granular avalanches: DEM simulation and comparison with experiment. Granular Matter, **11**(4): 209–220.

Teufelsbauer, H., Wang, Y., Pudasaini, S. P., Borja, R. I., and Wu, W. 2011. DEM simulation of impact force exerted by granular flow on rigid structures. Acta Geotechnica, **6**: 119–133.

Thielicke, W., and Stamhuis, E. J. 2014. PIVlab – Towards User-Friendly, Affordable and Accurate Digital Particle Image Velocimetry in MATLAB. Journal of Open Research Software **2**(1), e30, Ubiquity Press, Ltd., Oct. 2014. DOI: 1.5334/jors.bl.

VanDine, D. F. 1996. Debris flow control structures for forest engineering, 1996. Res. Br., British Columbia Ministry of Forests, Victoria, B.C., Working Paper 08/1996.

Wang, F., Cheng, X-Q., and Chen, J-G. 2017a. Experimental study on the energy dissipation characteristics of debris flow deceleration baffles. Journal of Mountain Science, **14**(10): 1951–1960.

Wang, F., Chen, X-Q., Chen, J-G., and You, Y. 2017b. Experimental study on a debris-flow drainage channel with different types of energy dissipation baffles. Engineering Geology, **220**: 43–51.

Wang, J.-P., Zeng, G.-H. and Yu, Hai-Sui. 2019. A DEM investigation of water-bridged granular materials at the critical state. Computational Particle Mechanics, **6**: 637–655.

Wyllie, D. C. 2014. Rock fall engineering: development and calibration of an improved model for analysis of rock fall hazards on highways and railways. PhD thesis, University of British Columbia, Canada.

Yong, A. C. Y., Lam, C. Lam, N. T. K., Perera, J. S. and Kwan, J. S. H. 2019. Analytical solution for estimating sliding displacement of rigid barriers subjected to boulder impact. Journal of Engineering Mechanics, **145**(3): 04019006.

Zhao, J., and Shan, T. 2013. Coupled CFD-DEM simulation of fluid-particle interaction in geomechanics. Powder Technology, **239**: 248–258.

Zhou, G. G. D., and Ng, C. W. W. 2010. Numerical investigation of reverse segregation in debris flows by DEM. Granular Matter, **12**(5): 507–516.

Zhou, G. G. D., Du, J., Song, D., Choi, C. E., Hu, H. S., and Jiang, C. 2020. Numerical study of granular debris flow run-up against slit dams by discrete element method. Landslides, **17**: 585–595.

List of notation

a	Acceleration
$A_{boulder}$	Cross-sectional area of boulder
A_{flow}	Cross-sectional area of flow
B	Channel width
C_n	Contact identification number
D_{baf}	Contact durability for flow interacting with baffles
D_{open}	Contact durability for flow in channel without obstacles ('open-channel')
e	Coefficient of restitution
F	Force
F_{flow}	Force on a barrier due to bulk flow material
F_{peak}	Peak force on a barrier
F_{static}	Final static force on a barrier
Fr	Froude number (sampled at flow front unless otherwise stated)
Fr_{min}	Minimum Froude number
g	Gravitational acceleration
h	Flow depth
h_1	Flow depth before impact
h_2	Flow depth after impact (i.e. pileup height)
ID	Identification number of individual grains
k	Earth pressure coefficient
k_{shape}	Shape-dependent parameter
KE	Kinetic energy
L	Characteristic length
L_C	Length of sloped channel after perch
L_H	Length of hopper
L_{mon}	Length of monitoring section
m	Grain mass
N_{gr}	Number of grains in a monitoring region
r	Particle radius
s	Spacing between baffles
t	Time
t_{step}	Timestep
Q	Flow rate
Q_{baf}	Flow rate for flow interacting with baffles
Q_{open}	Flow rate for flow in channel without obstacles ('open-channel')
U	Velocity
U_0	Velocity before impact
$V_{boulder}$	Volume of boulder
x	x-position down the channel
α	Semi-empirical impact coefficient
δ	Particle diameter
δ_{95}	95th percentile of particle diameter (i.e. 95% of the material in the sample is finer than this size)
δ_{bed}	Equivalent characteristic particle size of rough bed
$\delta_{boulder}$	Diameter of boulder
δ_{bulk}	Diameter of particles making up the bulk part of a flow
δ_{max}	Maximum particle diameter in a flow (typically boulders in this manuscript)
Δt	Impact time

θ Channel inclination
μ_{max} Friction angle between boulder and channel base
ρ Bulk density
ρ_s Boulder density
ρ_f Density of bulk granular assembly (assuming it to be an equivalent fluid)

Appendix I

The flow front governs interaction between flows and obstacles (Ng *et al.* 2019), so a measuring section that moves and deforms with the frontal 10% of the flow was adopted for characterising flow properties:

$$h = \frac{2}{N_{\mathrm{gr}}} \sum_{i=1}^{N_{\mathrm{gr}}} h_i \tag{A1}$$

$$U = \frac{1}{N_{\mathrm{gr}}} \sum_{i=1}^{N_{\mathrm{gr}}} U_i \tag{A2}$$

$$Fr = \frac{U}{\sqrt{gh\cos\theta}} \tag{A3}$$

$$\nu = \frac{N_{\mathrm{gr}} \frac{4}{3}\pi r^3}{hBL_{\mathrm{mon}}} \tag{A4}$$

where N_{gr} is the number of particles in the measuring volume; h_{i} is the height of the centroid of particle i; U_{i} is the velocity of particle i; r is the particle radius; B is the channel width; and L_{mon} is the length of the measuring section, which can vary during outflow. Eqn. (A1) finds the flow depth by doubling the average flow depth. (This is preferable to using a simple maximum value, which is easily distorted by saltating particles). Eqn. (A2) is a mean of the particle velocities in the monitoring region. In Eqn. (A3), a Froude number is computed for all the particles in the measuring region based on Eqns. (A1) and (A2). Eqn. (A4) obtains the volume fraction by dividing the total volume of the particles within the monitoring region by the estimated bulk flow volume.

The flow depth, velocity, Froude number and solid volume fraction for six open-channel flows with varying channel length L are shown in Fig. A1. Fig. A1a shows an example of how Fr at the flow front changes as the flow moves down the channel; L was 11 m. Fr at the flow front increases from just over 2 after the perch to a maximum of around 4 at the transition point between the sloped channel and the horizontal channel. Fr then decreases in the horizontal channel at two distinct rates. The initial steep drop occurs due to energy dissipated through impact with the horizontal channel. The secondary drop occurs due to shearing with the base of the horizontal channel. For this case, Fr measured at the position where the first row of baffles would have been on the horizontal plane was measured to be

around 3.3. *Fr* of 3.3 can also be found on the sloped channel, 4.4 m away from the start of the channel. This point is selected for the first row of baffles on the slope to ensure dynamic similarity for comparing cases where the array is on the slope and on the horizontal.

This exercise was repeated for several different channel lengths using open channels (Fig. A1b). *Fr* for three locations are shown: at the transition between the slope and the horizontal, the start of where the array of baffles would have been placed on the horizontal channel, and where the barrier would have been. It is worth noting that the *Fr* attained are within the nominal range for debris flows suggested by Hübl *et al.* (2009).

Fig. A1c shows the position for the start of the baffle array on the slope as determined from *Fr* curves (e.g. Fig. A1a), to ensure that cases with baffles on the slope and on the horizontal are dynamically comparable. Fig. A1d shows the velocity and flow depth at the flow front for different *Fr*.

Appendix II

Fig. A2a is modified from Goodwin and Choi (2020) and shows the algorithm used for determining contact duration. LIGGGHTS saves contact data for every particle in the simulation domain at a specified interval, including the IDs of particles in contact, as well as their spatial position. The algorithm firstly imports the contact data and then sorts contacts by their position along the channel; only the frontal 10% of particles are retained. This is equivalent to having a monitoring section that moves and deforms with the flow.

For each time step considered, pairs of IDs of particles that are in contact are recorded. This list of ID pairs is then compared against the particles in contact at the next time step. The number of ID pairs (i.e. contacts) that exist in both lists are divided by the total number of contacts in the first list. This gives a number between zero, meaning no sustained contacts, and unity, meaning all contacts are sustained.

Fig. A2b shows an idealised 2D schematic of this process for a small number of particles across two time steps. In the region shown, at the first time step, there are seven pairs of particles in contact. The contact IDs (‘2 – 5’, ‘4 – 5’, ‘5 – 6’ etc.) are recorded. At the second time step, there are also seven contacts, of which five also appeared in the previous time step. The contact durability for this region would therefore be computed as 5/7 = 0.71. (Note that for the actual simulations, the domain is 3D.)

Table 1: Summary of recommendations for baffle design from various international guidelines

Guidelines	Objectives given	Baffle spacing	Number of rows of baffles	Baffle spacing: downstream	Other aspects of baffle design	Baffle placement
Vandine (1996) [Canada]	Decelerate granular flow and cause deposition; deflect trajectory of flow.	-	-	-	-	Suggests that baffles are more commonly placed in [nearly-horizontal] deposition areas.
FHWA (2006) [USA]	Decelerate fluvial flow; prevent acceleration of flow during vertical drop; have greater control over the hydraulic jump; enable stilling basins to be made smaller.	Baffle width and horizontal baffle spacing should be 1.5*H*.	States that four rows of baffles can 'control the flow' but that fewer rows can also be 'successful'.	Downstream spacing of baffles on a 27° slope should be 2*H*, whilst on lower gradients the spacing can be larger.	(*i*) Baffle height should be 0.8 times the critical depth; (*ii*) baffles should be staggered.	Schematics show that baffles can be placed on slope or on the horizontal.
Jóhannesson *et al.* (2009) [EU]	Decelerate and break up avalanches.	Mounds should be 'close together'.	Authors suggest one row of mounds should reduce velocity by 20%, whilst a second row reduces velocity by a further 10%.	Mounds should be 'close together'.	(*i*) Height should be 2–3 times that of the dense avalanche core; (*ii*) upstream face of baffle should be 'steep' (>60°); (*iii*) aspect ratio of upstream face should be around unity.	Implied to be on slopes.
Kwan *et al.* (2018) [Hong Kong]	Filtering out boulders; reducing the load on a terminal barrier.	Document implies range $1.5 < s/\delta < 4.0$, based on other recommendations from other countries.	No guidance given. The example case given contains two rows of baffles.	Based on the trajectory of an idealized point mass overflowing the array if a plug forms between the baffles.	(*i*) Baffle height should be 'sufficiently high to intercept boulders'; (*ii*) gives an equation for calculating energy dissipation of the baffle due to formation of a plastic hinge, as well as bending moment; (*iii*) suggests that sliding and overturning failure should be considered in design; (*iv*) baffle arrays proposed for reducing force on terminal barriers, but not quantitative.	Placement not explicitly mentioned, although the example in the guidelines shows them on a horizontal plane in front of a barrier.

Table 2a: Summary of previous studies on baffles or baffle-like objects

Studies	Objective(s) (not exhaustive)	Study type	Material	Baffle placement	Baffle spacing: lateral (m)	δ_{95}	s/δ	Number of rows of baffles	Baffle spacing: downstream (m)
Hákonardóttir *et al.* (2003a)	Overflow trajectory	Physical	Snow	Orthogonal to slope	0.400	< 0.1	> 4	1	
Hákonardóttir *et al.* (2003b)	Trajectory, velocity and energy reduction	Physical	Glass beads	Orthogonal to slope	0.030	0.0001	300	1	
Cosenza *et al.* (2006)	Model evaluation and baffle deformation	Finite volume: shallow water		Orthogonal to runout zone				4	
Teufelsbauer *et al.* (2011)	Deposition and impact force on a final obstacle	DEM		Orthogonal to slope	0.090	0.005	18	7	0.01
Ng *et al.* (2014)	Velocity and energy reduction	Physical tests and DEM	LB sand	Orthogonal to slope	0.046–0.080	0.0006	80–130	1	
Choi *et al.* (2014)	Velocity and energy reduction	Physical tests	LB sand	Orthogonal to slope	0.047	0.0006	80	1–3	0.05–0.10
Ng *et al.* (2015)	Velocity and energy reduction	Physical tests	LB sand	Orthogonal to slope	0.080	0.0006	80–130	3	0.05–0.10
Choi *et al.* (2015)	Velocity and energy reduction	DEM		Orthogonal to slope	0.047	0.005	9.4	1–2	0.05–0.25
Law *et al.* (2015)	Force reduction	DEM		Orthogonal to slope	0.080	0.005	16	1–2	0.056–0.344
Silva *et al.* 2016	Trapping	Physical flume and CFD-DEM	Mixture of rocks and water	Orthogonal to slope	0.04–0.07	0.04	0.92–1.77	1	
Wang *et al.* 2017a	Velocity and energy reduction, deposition	Physical flume	Mixture of water, sand and clay	Orthogonal to slope	0.050	0.02	2.5	3	0.10–0.25
Wang *et al.* 2017b	Velocity and energy reduction, baffle shape	Physical flume	Mixture of water, sand and clay	Orthogonal to slope	0.050	0.02	2.5	3	0.10–0.25
Leonardi *et al.* (2018)	Back-analysis of rheology	Lattice-Boltzmann method		Orthogonal to slope				2	
Bi *et al.* (2018a)	Force on baffles and barrier	DEM		Orthogonal to slope	6–12			4	6–30
Bi *et al.* (2018b)	Energy reduction	DEM		Orthogonal to slope	4–12			5	4–28
Kim *et al.* (2019)	Velocity and energy reduction	Physical tests	Jumunjin sand	Orthogonal to slope	0.075	0.009	8.3	1–4	0.2
Fei *et al.* (2020)	Velocity and energy reduction, deposition	Physical tests	Sand	Orthogonal to runout zone	0.070	0.001–0.02	3.5–70	2–3	0.07
Goodwin and Choi (2020)	Trapping	Physical flume / DEM	Dry glass beads	Orthogonal to slope	0.020–0.160	0.01	2–16	1	
Li *et al.* (2020)	Energy reduction	Material Point Method		Orthogonal to slope	4–8			1–3	8–12

Table 2b: Summary of previous studies on baffles or baffle-like objects (continued)

Studies	**Baffle height** (m)	**Flow depth** (m)	**Landslide volume** (m^3)	**Landslide debris density** (kg/m^3)	**Slope** (°)	**Channel length** (m)	**Channel width** (m)	**Relevant findings** (not exhaustive)
Hákonardóttir *et al.* (2003a)	0.4–0.6	0.2–0.4	5		45	34	2.5	
Hákonardóttir *et al.* (2003b)	0.03	0.01	0.004	1600	37	6	0.05	Flow velocity reduced by 40%
Cosenza *et al.* (2006)				1600				
Teufelsbauer *et al.* (2011)	0.05		0.0006	1400			1.1	
Ng *et al.* (2014)	0.12	0.08	0.06	1680	26	5	0.2	KE reduced by 25 to 55%.
Choi *et al.* (2014)	0.06–0.12	0.08	0.06	1680	26	5	0.2	KE reduced by 30 to 75%
Ng *et al.* (2015)	0.06–0.1	0.08	0.06	1680	26	5	0.2	Flow velocity reduced by 30 to 60%
Choi *et al.* (2015)	0.06–0.12	0.08	0.04	1600	26	5	0.2	KE reduced by 20 to 80% depending on number of rows of baffles and height.
Law *et al.* (2015)	0.03–0.10	0.04	0.04	1600	35	-	0.2	Force on a terminal barrier reduced by 55 to 65%
Silva *et al.* 2016	> 0.5		0.5		6–11	3.5	0.5	Trapping efficiency very sensitive to s/δ for s/δ less than around 3
Wang *et al.* (2017a)	0.050	0.14		1200–2100	9–15	6	0.4	Reported velocity reduction: 12–39
Wang *et al.* (2017b)	0.025–0.050	0.14		1200–2100	12	6	0.4	Reported velocity reduction: 3–30
Leonardi *et al.* (2018)			600	2210		250		
Bi *et al.* (2018a)	6	6	18		20	60–200	84	Impact force on baffles: fourth row is half of first row. Impact force on downstream barrier reduced by half with four rows of baffles.
Bi *et al.* (2018b)	10		3.6					
Kim *et al.* (2019)	0.02–0.08	0.03–0.05	0.05		29	4.8	0.3	Velocity reduction: 45 to 70% in average
Fei *et al.* (2020)	0.05	0.02–0.05	0.02	1260–1350	30	1.2	0.3	
Goodwin and Choi (2020)	0.5	0.060–0.075	0.01	1600	22–30	5	0.2	Trapping efficiency very sensitive to s/δ for s/δ less than around 3
Li *et al.* (2020)	4		11000	2000	50	100	60	

Table 3: Parameters adopted in numerical simulations

	Numerical simulations	**Reference**
Particle density (kg/m^3)	2650	-
Internal friction angle (°)	20	Ng *et al.* (2019)
Interface friction angle (°)	17	Choi *et al.* (2016)
Elastic modulus (Pa)	10^8	Ng *et al.* (2019)
Poisson's ratio	0.3	
Rolling resistance	0	
Contact model	Hertz	
Coefficient of restitution	0.5	See text

Table 4: Test plan

Series	**Baffle array location**	**Baffle spacing** ($s/\delta_{\text{boulder}}$)	**No. of rows of baffles**	**Barrier?**	**Channel length** (m)
Granular flow only	-	-	0	No	5, 9, 11, 17, 23, 29, 35, 41, 47
Granular flow + boulders	-	-	0	Yes	7, 8, 9, 11, 17, 23, 29, 35, 41
	Sloped channel	1, 2, 4	3		11, 17, 23, 29, 35, 41
	Horizontal channel				7, 8, 9, 11, 17, 23, 29, 35, 41

Fig. 1: Arrays of baffles installed in Hong Kong SAR. (a) Near New Territories Circular Road on a slope; (b) installed in front of a rigid barrier on a near-horizontal plane.

Fig. 2: Physical & numerical setups for the calibration exercise. (a) Oblique view of flume; (b) plan view of the roughened base and slit-structure; (c) downstream view of roughened base and slit-structure; (d) side-view schematic of the physical & DEM setups; (e) plan-view schematic of the physical & DEM setups.

Fig. 3: Comparison of (a) physical flow kinematics with PIV vectors overlaid; and (b) computed flow kinematics, also with PIV vectors overlaid. Frames are separated by 0.2 s: (*i*) $t = 0.0$ s; (*ii*) $t = 0.2$ s; (*iii*) $t = 0.4$ s; (*iv*) $t = 0.6$ s; (*v*) $t = 0.8$ s; (*vi*) $t = 1.0$ s. The slit width s was 50 mm, giving $s/\delta = 5$.

Fig. 4: Comparison of physical and computed flow characteristics. (a) Maximum pile-up height at the slit-structure normalized by the maximum depth of flows in channels without obstacles; (b) average outflow rate of the flow from the slit-structure. $Fr_{\min}$ was taken from a series of flows in channels without obstacles (see Choi *et al.* 2016).

Fig. 5. Numerical setup for the simulations with both a fine granular assembly and a set of perched boulders. The length of the flat section on which the boulders are initially perched is 1 m. Separate cases are run where the baffle array is placed on the horizontal channel (parts (a) and (c)) and the slope (parts (b) and (d)).

Fig. 6: Flow kinematics for two cases:
(a) Flow & boulders with baffles on a slope;
(b) Flow & boulders with baffles on the horizontal channel (directly in front of the barrier).
Times for frames: (*i*) 0.0 s; (*ii*) 0.8 s; (*iii*) 1.6 s; (*iv*) 2.4 s; (*v*) 3.2 s; (*vi*) when system has come to rest. For both cases, the ratio $s/\delta_{\text{boulder}}$ is 1.0. The colouring of the grains corresponds to velocity.

Fig. 7: Normalised average outflow velocity for flows passing through arrays of baffles. (a) and (b) show measuring regions after the first and third rows of baffles for an array on the slope, respectively; (c) and (d) are for arrays on baffles on the horizontal plane.

Fig. 8: Normalised peak outflow rates for $s/\delta = 1.0$ to 4.0, and for baffle configurations on the slope and on the horizontal plane. Outflow is measured after (a) the first row of baffles; (b) the third row of baffles. The measuring regions are indicated schematically.

Fig. 9: Normalised contact durability comparing flows in channels with and without baffles.

Fig. 10: Normalised force on the barrier for a mixture of boulders and a bulk granular assembly: (a) baffles on the slope; (b) baffles on the horizontal channel. *Fr* corresponds to the condition before impact with the first row of the baffle array,

whilst k is taken as unity. Insets show zoomed-in versions of certain parts of the graph.

Fig. A1: Calibration exercise for characterizing *Fr* for channels without obstacles. The purpose is to ensure dynamically similar impacts for flows impacting baffles on the slope and on the horizontal plane. (a) Example of *Fr* at flow front for an open-channel flow for a channel length L_c of 11 m. (b) *Fr* at the flow front at various points of interest along the open channel, for varying channel lengths. (c) Computed position of the baffle array on the slope (relative to the start of the slope). This is determined by matching *Fr* for where the baffle array would be on the horizontal plane. (d) Flow depth and flow velocity at the front of the flow for a series of *Fr* for where the baffles would be.

Fig. A2: Calculation of contact durability (see Fig. 9). (a) Algorithm for contact duration (modified from Goodwin and Choi 2020); (b) idealised two-dimensional schematic of particle contacts for two time steps (also modified from Goodwin and Choi 2020). Numbers in black indicate particle ID, whilst numbers in red indicate pairs of particles in contact.

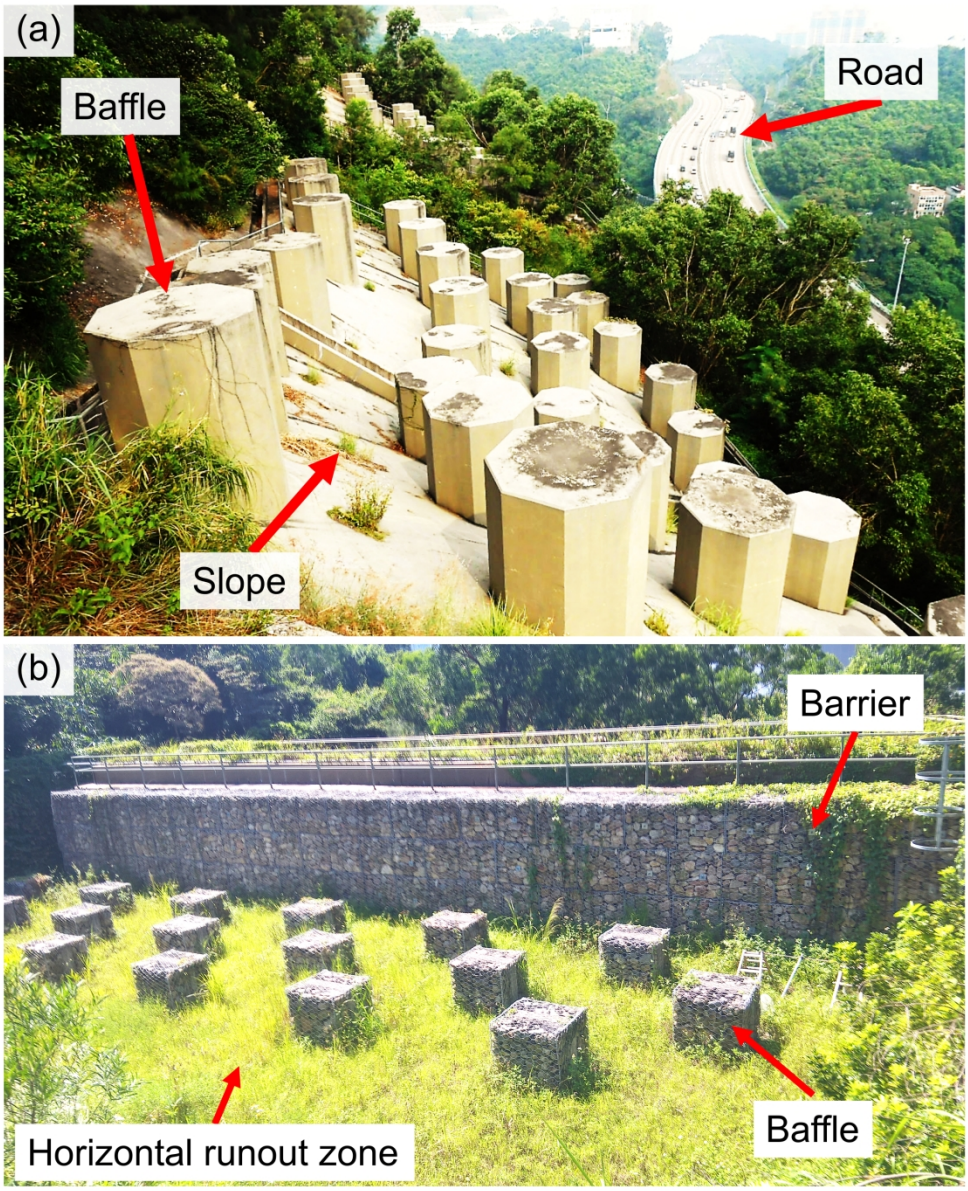

Fig. 1: Arrays of baffles installed in Hong Kong SAR. (a) Near New Territories Circular Road on a slope; (b) installed in front of a rigid barrier on a near-horizontal plane.

860x1050mm (72 x 72 DPI)

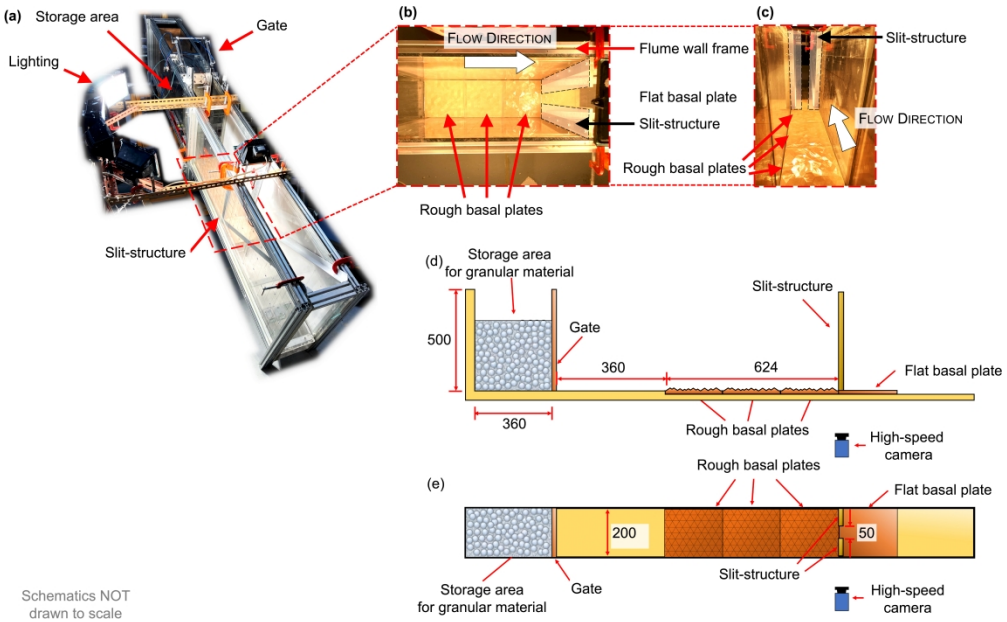

Fig. 2: Physical & numerical setups for the calibration exercise. (a) Oblique view of flume; (b) plan view of the roughened base and slit-structure; (c) downstream view of roughened base and slit-structure; (d) side-view schematic of the physical & DEM setups; (e) plan-view schematic of the physical & DEM setups.

2822x1728mm (72 x 72 DPI)

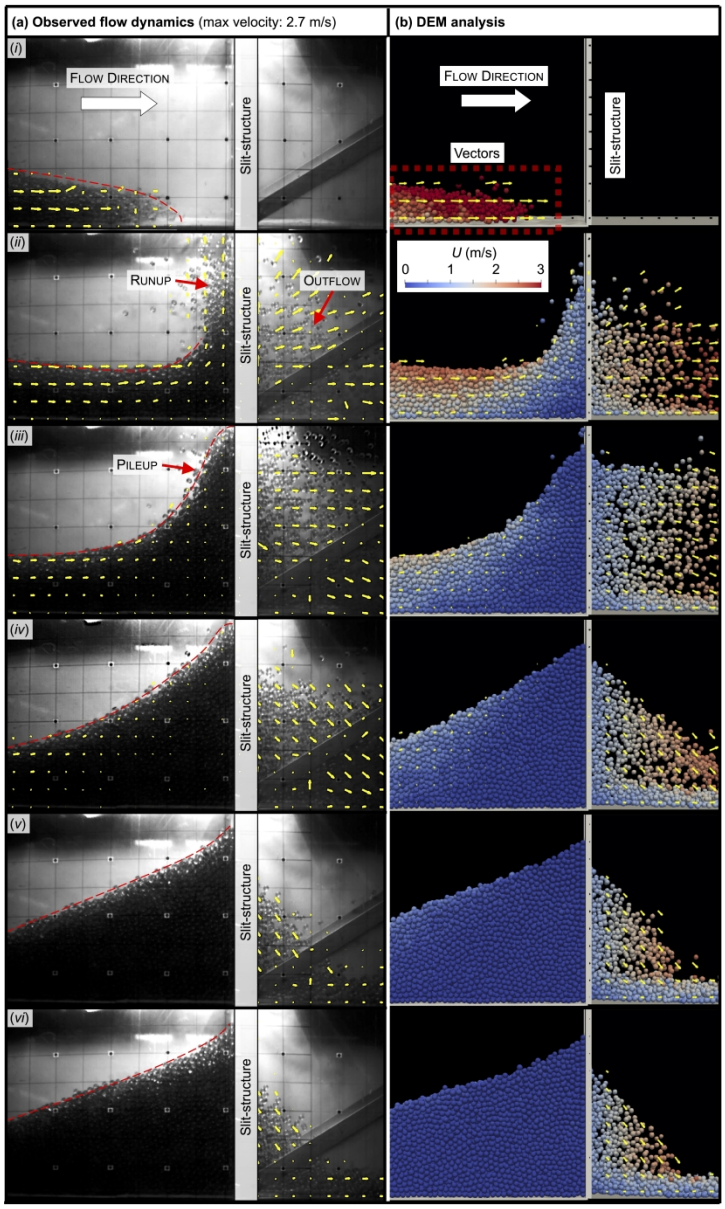

Fig. 3: Comparison of (a) physical flow kinematics with PIV vectors overlaid; and (b) computed flow kinematics, also with PIV vectors overlaid. Frames are separated by 0.2 s: (i) t = 0.0 s; (ii) t = 0.2 s; (iii) t = 0.4 s; (iv) t = 0.6 s; (v) t = 0.8 s; (vi) t = 1.0 s. The slit width s was 50 mm, giving s/δ = 5.

1693x2828mm (72 x 72 DPI)

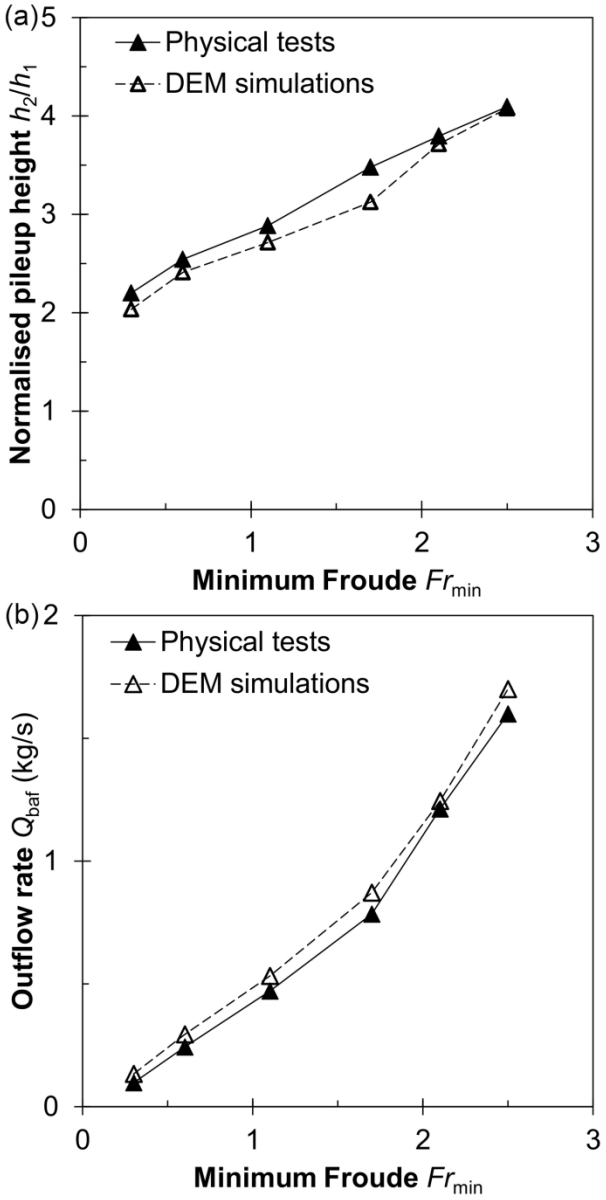

Fig. 4: Comparison of physical and computed flow characteristics. (a) Maximum pile-up height at the slit-structure normalized by the maximum depth of flows in channels without obstacles; (b) average outflow rate of the flow from the slit-structure. Frmin was taken from a series of flows in channels without obstacles (see Choi et al. 2016).

122x241mm (300 x 300 DPI)

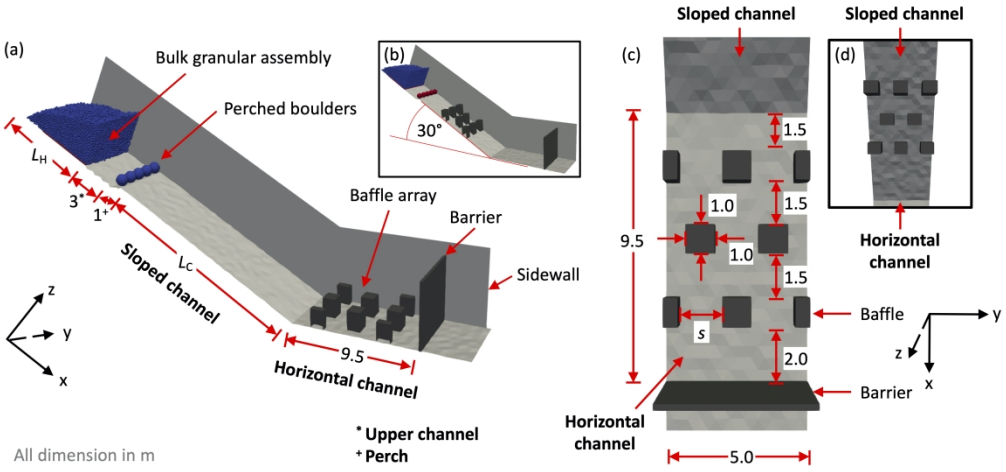

Fig. 5. Numerical setup for the simulations with both a fine granular assembly and a set of perched boulders. The length of the flat section on which the boulders are initially perched is 1 m. Separate cases are run where the baffle array is placed on the horizontal channel (parts (a) and (c)) and the slope (parts (b) and (d)).

338x156mm (300 x 300 DPI)

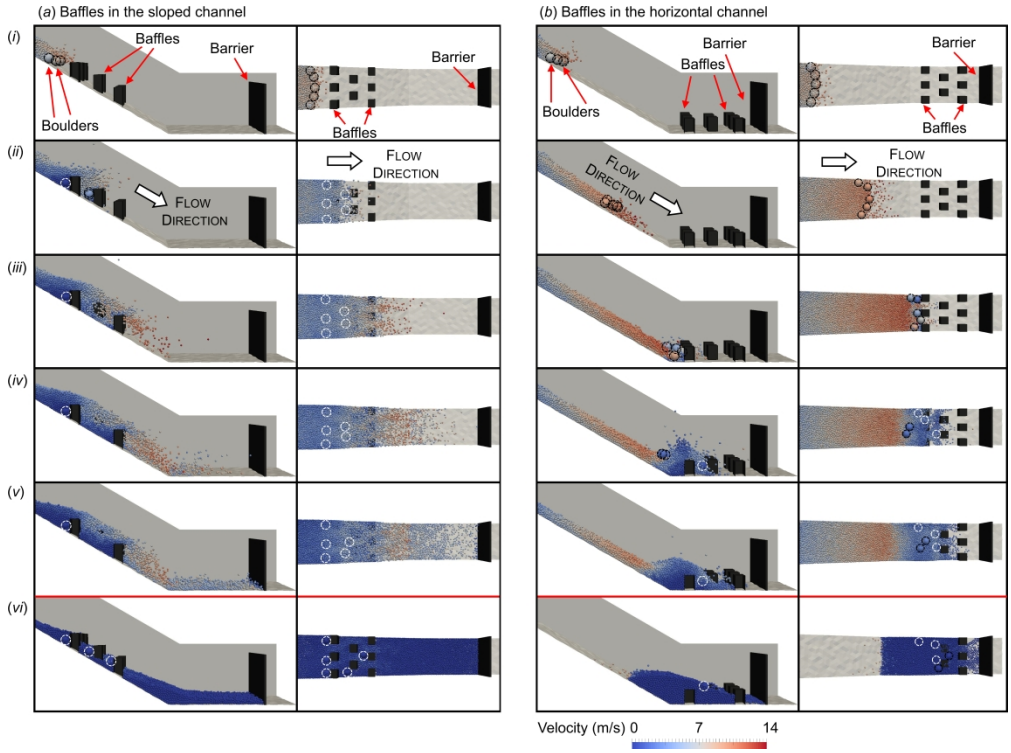

Fig. 6: Flow kinematics for two cases:
(a) Flow & boulders with baffles on a slope;
(b) Flow & boulders with baffles on the horizontal channel (directly in front of the barrier).
Times for frames: (i) 0.0 s; (ii) 0.8 s; (iii) 1.6 s; (iv) 2.4 s; (v) 3.2 s; (vi) when system has come to rest.
For both cases, the ratio s/□ boulder is 1.0. The colouring of the grains corresponds to velocity.

2565x1905mm (72 x 72 DPI)

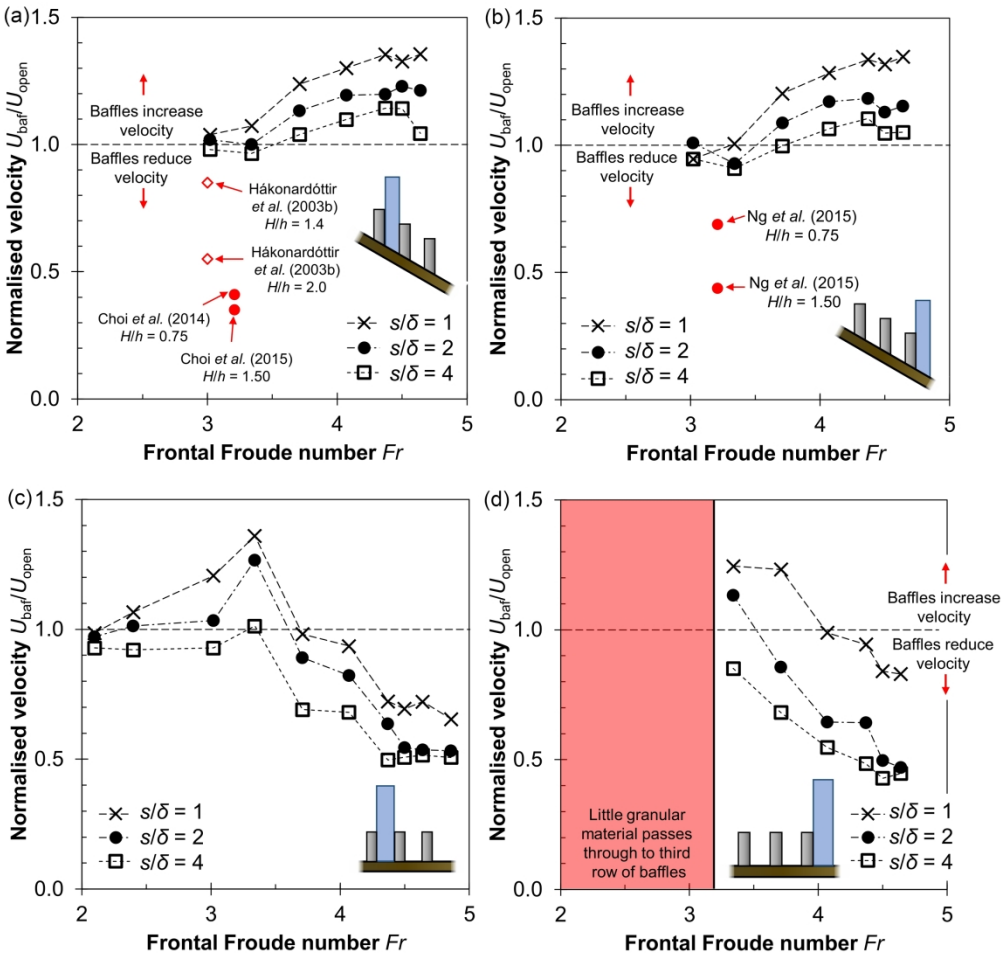

Fig. 7: Normalised average outflow velocity for flows passing through arrays of baffles. (a) and (b) show measuring regions after the first and third rows of baffles for an array on the slope, respectively; (c) and (d) are for arrays on baffles on the horizontal plane.

266x255mm (300 x 300 DPI)

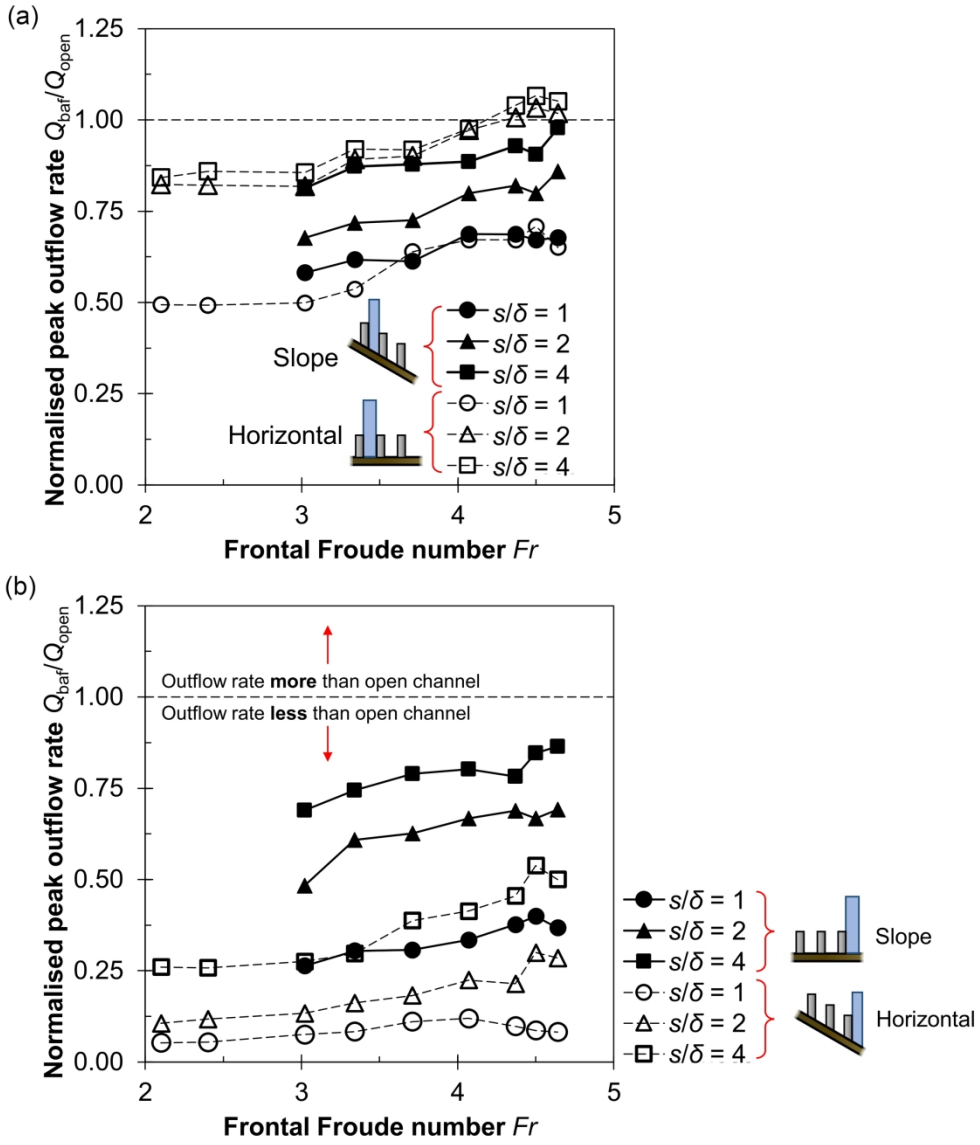

Fig. 8: Normalised peak outflow rates for s/□ = 1.0 to 4.0, and for baffle configurations on the slope and on the horizontal plane. Outflow is measured after (a) the first row of baffles; (b) the third row of baffles. The measuring regions are indicated schematically.

220x254mm (300 x 300 DPI)

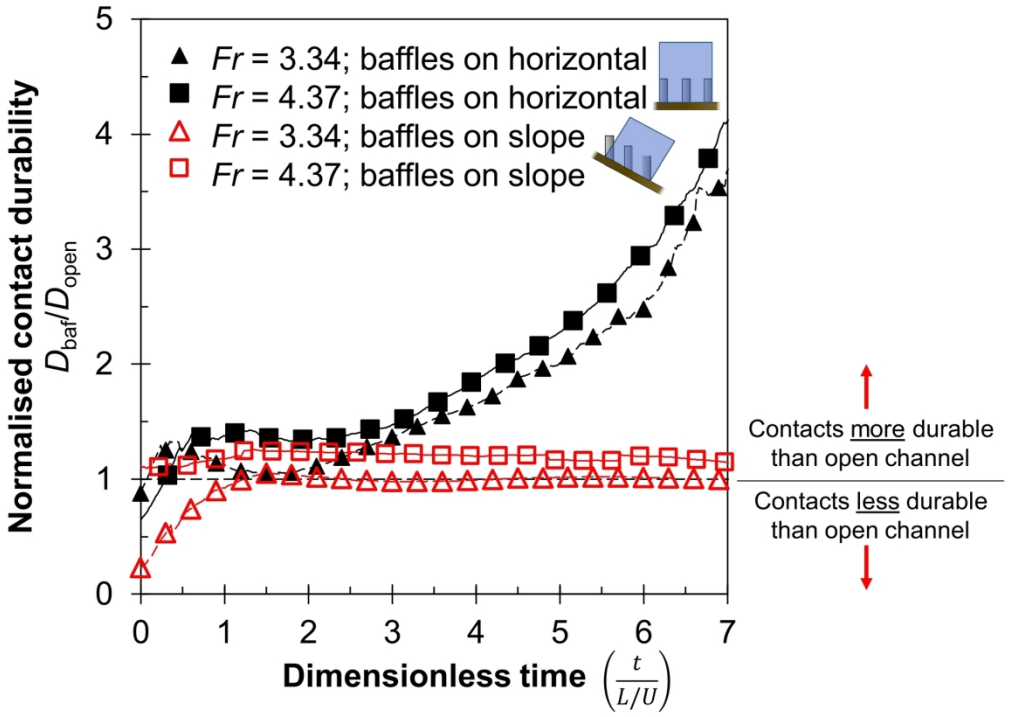

Fig. 9: Normalised contact durability comparing flows in channels with and without baffles.

174x125mm (300 x 300 DPI)

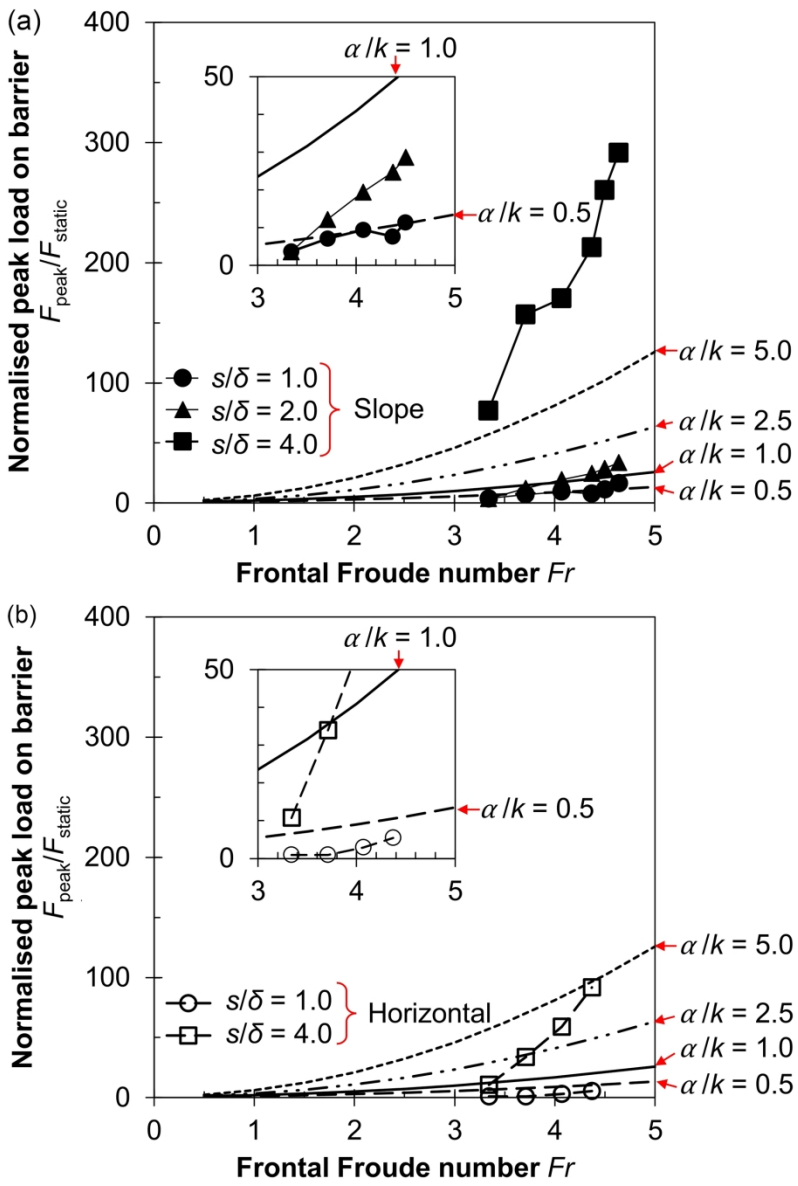

Fig. 10: Normalised force on the barrier for a mixture of boulders and a bulk granular assembly: (a) baffles on the slope; (b) baffles on the horizontal channel. Fr corresponds to the condition before impact with the first row of the baffle array, whilst k is taken as unity. Insets show zoomed-in versions of certain parts of the graph.

166x245mm (300 x 300 DPI)

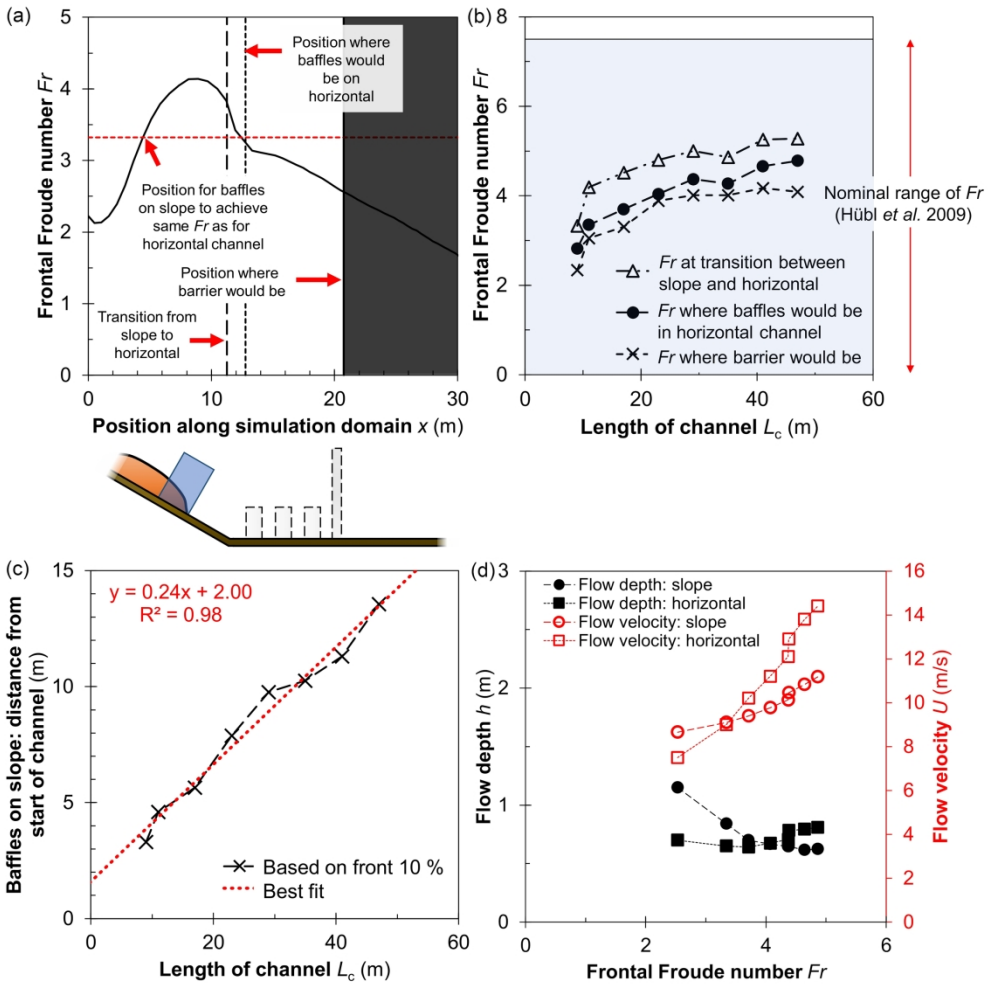

Fig. A1: Calibration exercise for characterizing Fr for channels without obstacles. The purpose is to ensure dynamically similar impacts for flows impacting baffles on the slope and on the horizontal plane. (a) Example of Fr at flow front for an open-channel flow for a channel length Lc of 11 m. (b) Fr at the flow front at various points of interest along the open channel, for varying channel lengths. (c) Computed position of the baffle array on the slope (relative to the start of the slope). This is determined by matching Fr for where the baffle array would be on the horizontal plane. (d) Flow depth and flow velocity at the front of the flow for a series of Fr for where the baffles would be.

225x224mm (300 x 300 DPI)

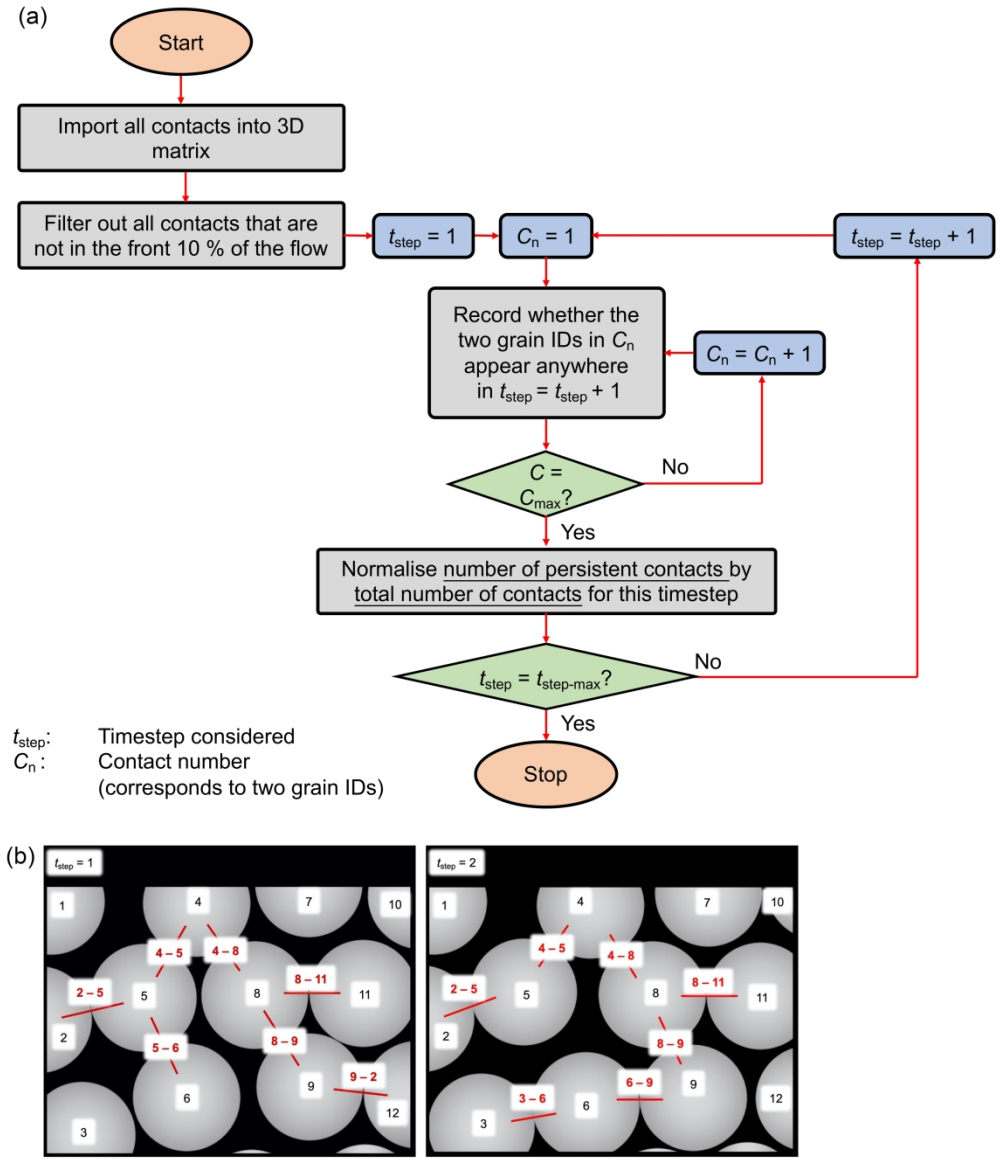

Fig. A2: Calculation of contact durability (see Fig. 9). (a) Algorithm for contact duration (modified from Goodwin and Choi 2020); (b) idealised two-dimensional schematic of particle contacts for two time steps (also modified from Goodwin and Choi 2020). Numbers in black indicate particle ID, whilst numbers in red indicate pairs of particles in contact.

297x346mm (300 x 300 DPI)